이학박사학위논문

나노다공성 인듐 주석 산화물 전극에서의 구조 효과 연구 및 바이폴라 전극 센서로의 응용

Morphological Effects of Nanoporous Indium Tin Oxide Electrodes towards Electron Transfer and Its Applications as Bipolar Electrode Sensors

2020 년 2 월

서울대학교 대학원

화학부 전기분석화학전공

서 민 지

A Ph. D. Dissertation

Morphological Effects of Nanoporous Indium Tin Oxide Electrodes towards Electron Transfer and Its Applications as Bipolar Electrode Sensors

By

Minjee Seo

February 2020

Supervisor: Professor Taek Dong Chung

Major: Electrochemistry

School of Chemistry

Graduate School of

Seoul National University

Abstract

Along with the fast development of technology and the advent of environmental issues, the need for efficient and cost-effective electrocatalysts used in energy devices and sensors have increased greatly. Numerous researches have focused on improving the efficiency of electrocatalysts while reducing the contents of noble metals. In this context, fabricating nanostructured catalysts in order to enhance its catalytic activity has long been crucial in electrocatalyst development. In particular, nanoporous electrodes are widely utilized as competent catalysts due to its enlarged surface area and catalytic active surface characteristics. The catalytic contribution from an additional catalytic factor arising from the nanoporous morphology (nanoconfinement effects) has been suggested and investigated by several groups, most of which have utilized noble metal based nanoporous electrodes. In this thesis, nanoconfinement effects were investigated by employing low catalytic material with systematically varied nanoporous layer thickness. Furthermore, the effect of structure modification towards sensor sensitivity were demonstrated.

In the first part of the thesis, the acceleration of electron transfer kinetics at the nanoporous indium tin oxide (ITO) electrodes were investigated. In this study, the catalytic activity of nanoporous electrodes was explored regarding the effects of confined morphology of the electrode towards heterogeneous electron transfer reactions. In order to observe the geometric contribution towards the electrocatalytic activity, ITO was chosen as the electrode material due to its low catalytic activity. Systematically varying the nanoporous ITO layer thickness allowed the exclusion of surface-originated catalytic effects of the nanoporous electrodes such as defect densities. Experimental results showed that the single electron transfer of $Fe^{2+/3+}$ that

involve no proton transfer is more facilitated with thickening ITO nanoporous layers, which have higher proportion of nanoconfined geometry.

In the second part of the thesis, a novel indium-tin oxide (ITO) bipolar electrode (BPE) based sensor by the implementation of nanoporous ITO, is introduced. The nanoporous ITO layer implemented BPE showed markedly enhanced ECL signals compared to the planar ITO based BPE, enabling the detection of H_2O_2 even under a mild operating voltage. The ECL calibration curves towards H_2O_2 detection using BPEs of various nanoporous layer thicknesses exhibited lowered LODs and improved sensitivities with thickening nanoporous layers. We speculate that the nanopore morphologies may have spatially confined the analytes, thus leading to amplified ECL signals.

Keywords: electrocatalyst, nanoporous electrode, confinement effect, electrochemical impedance spectroscopy, bipolar electrode

***Student number*:** 2014-21241

Contents

2. Investigation of Nanoconfinement effects at Nanoporous Indium Tin Oxide Electrodes

3. Nanoporous ITO implemented Bipolar Electrode Sensor for enhanced Electrochemiluminescence

List of Figures

Figure 2-3 Cyclic voltammograms of ITO x1, ITOx2, ITO x3, ITO x4 and ITO x6 electrodes measured in 10 mM Fe(II)SO_4 / 100 mM H_2SO_4 / 500 mM K_2SO_4 solution, where the current density in the y-axis is the current divided by the geometric surface area of the electrode. The scan rate is 50 mV/s.

Figure 2-4 (a) Randles equivalent circuit that was used in fitting the EIS results. (b) An example of EIS fitting result with the equivalent circuit shown in (a), using the EIS data of ITO x2 electrode measured in 10 mM Fe(II)SO_4 + 5 mM Fe(III) SO_4 / 100 mM H_2SO_4 / 500 mM K_2SO_4.

Figure 2-5. The charging current of nanoporous ITO electrodes obtained by cyclic voltammetry in the absence of the redox species $Fe^{2+/3+}$ (100 mM H_2SO_4 / 500 mM K_2SO_4). The scan rate is 50 mV/s. The charging current values displayed in Table 2-2 were obtained by averaging the value of anodic and cathodic charging currents at 0.0 V (vs. Hg/$HgSO_4$, sat K_2SO_4).

Figure 2-6. The standard rate constant k^0 of the $Fe^{2+/3+}$ reaction from ITO x1 (orange), ITO x2 (blue), ITO x3 (green) and ITO x4 (red) nanoporous electrodes, which are calculated from equation 2 and 3. The average k^0 values and the respective standard errors were obtained from three different electrodes made with the same number of spin coating process.

Figure 2-7 Scheme illustrating the increasing proportion of 'confined space' with respect to 'non-confined space' as the nanoporous layer thickness increases.

Figure 2-8 (a) The standard rate constants (k^0) of ITO x1, ITO x2, ITO x3, ITO x4 and ITO x6 nanoporous electrodes obtained at 5 ℃ (blue), 12.5 ℃ (green), 20 ℃ (orange), and 27.5 ℃ (red). The k^0 is calculated from EIS data using the equations 2

and 3. All displayed k^0 values are normalized with respect to the roughness factor of each electrode. (b) Setting the k^0 of the nanoporous electrode (ITO x1) to be unity for all temperatures, the relative ratio of k^0 of thicker nanoporous electrodes (ITO x2, ITO x3 ITO x4 and ITO x6) is calculated and plotted.

Figure 2-9. Arrhenius plots of x1~x4 nanoporous ITO electrodes (above), and the corresponding activation energies (graph below).

Figure 3-1. Scheme of bipolar electrodes, where η_{cat} and η_{an} represent the cathodic and anodic overpotentials respectively.

Figure 3-2. (a) Diagram of the nanoporous BPE microchip. The upper right-hand figure depicts the top view of the BPE system, and the lower right-hand figure illustrates the cross section of the BPE system along line AB. The units of measurements are in mm. (b) Schematic diagram of the H_2O_2 sensing system based on the BPE. (η: overpotential applied on anodic poles of the BPE)

Figure 3-3 (a) Top view Field-Emission Scanning Electron Microscope (FESEM) image of a nanoporous ITO electrode spin coated 2 times. The figures (b-d) are the cross section FESEM images of electrodes spin coated (b) 2 times, (c) 3 times, and (d) 4 times. The scale bar represents 500 nm

Figure 3-4 (a) The charging currents of nanoporous ITO electrodes measured by cyclic voltammetry in 0.1 M phosphate buffered saline solution, where the scan rate is 50 mV/s. (b) The charging current values obtained by averaging the anodic and cathodic charging currents at 0.250 V (vs. Ag/AgCl (3 M NaCl)) are plotted against various scan rates (10, 20, 50, 100 mV/s). (c) Cyclic Voltammogram of bare ITO, ITO x2, ITO x3 and ITO x4 electrodes measured in 5 mM H_2O_2 / 0.1 M phosphate

buffered saline solution, scan rate 50 mV/s. (d) Electrochemical impedance spectroscopy (EIS) data of bare ITO, ITO x2, ITO x3 and ITO x4 electrodes measured in 5 mM H_2O_2 H_2O_2 / 0.1 M phosphate buffered saline solution, where the DC potential is -0.75 V.

Figure 3-5 H_2O_2 sensing system with four types of BPEs with different ITO nanoporous layer thicknesses. (a) ECL images obtained from with 5 mM H_2O_2 solution under operating voltage of 1.9 V (b) ECL intensities of BPEs obtained from 5 mM H_2O_2 solution depending on the operating voltage, where the inset shows the enlarged view of ECL intensities at mild operating voltages.

Figure 3-6 ECL intensities of x4 ITO implemented BPE depending on the applied voltage, measured in bare 0.1 M phosphate buffered saline solution.

Figure 3-7 Calibration curve of H_2O_2 detection showing ECL intensities depending on the analyte (H_2O_2) concentration. The dotted lines are added to guide the linear range of the calibration curve.

Figure 3-8 (a) ECL intensities of bareITO, ITO x2, x3, and x4 implemented BPEs, normalized by the relative ECSA values through the following equation; Normalized ECL intensity = {(Measured ECL intensity) – (Background ECL intensity)} / (ECSA value). The 'background ECL intensity', which is the light intensity under which no voltage is applied to the BPE, is subtracted to eliminate the background noise. (b) Possible scheme of reactants in the nanoconfined space of nanoporous ITO layers. The orange circles represent the reactant molecules, and the arrows represent simplified trajectories of the reactants. The blue, solid arrows demonstrate increased interaction between the reactant molecules and the electrode due to nanoconfinement

effects. The red dashed arrows depict reactants at the shallow regions of the nanoporous structure, which are less likely to be confined in the nanopores.

List of Tables

Chapter 1.

General Introduction

1.1 Background and Overview

1.1.1 Conventional approaches in developing electrocatalysts

Cost-effective and efficient electrocatalysts are in high demand in various fields, including energy conversion and storage devices. For example, oxygen reduction reaction (ORR) is of particular interest in fuel cells, where molecular oxygen goes through electrochemical reduction by four protons and electrons to form water. Due to its sluggish kinetics, fuel cell performances are often limited by the ORR, motivating many research towards improving the cathode efficiency. The "volcano plot" of catalysts [1,2] which correlate the intrinsic adsorption energy of the catalyst surface to its catalytic activity, have provided a guideline for the development of catalysts. The core of the volcano plot is that, for the optimal catalytic activity, the catalyst surface must bind the reactive intermediates with 'moderate' degree. As the binding energies of adsorbates largely depend on the electronic structure of catalyst surfaces, recent catalyst designs have focused on tuning the surface characteristics of catalysts. Pt alloys [2,3], or core-shell structures [4,5] lead to ligand effects or strain effects that change the interatomic distance of the surface atoms, resulting in altered d-band center and adsorption properties. Nanostructured catalysts also present promising strategies towards highly active catalysts, owing to their increase in surface roughness. For instance, nanoparticles [6], nanocage/frames [7,8], and nanoporous [9] catalysts display enhanced catalytic effects, which are mostly attributed to their increased density of surface defects, or exposure of high index facets.

However, the conventional approaches that aim to activate the catalyst surface through surface engineering bears several issues. First of all, optimization of surface adsorption properties tends to be based on noble metal materials, leading to high cost and scarcity issues [10]. This is mainly due to the sensitivity of reactant adsorption characteristics towards the electronic structure (surface atom arrangement) of the catalyst surface. Surface engineered catalysts also suffer from stability issues. For example, degradation of highly defective catalyst surfaces due to dissolution, or surface reconstruction towards stable surfaces [11,12], as well as leaching of less noble metals in platinum based alloys [13] have been reported. Furthermore, the highly adsorptive platinum surface may be susceptible towards poisoning by intermediates (e.g. CO) [14,15].

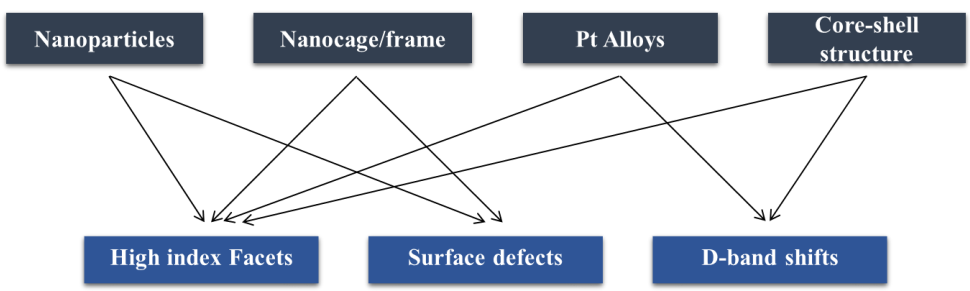

Figure 1-1. Conventional catalyst development strategies (upper line) and catalytic mechanism (lower line) electron transfer reaction. The major correlations are linked by arrows.

1.1.2 Chemistry in confined space

In this regard, an alternative strategy other than surface modification may be significant for the development of economical as well as efficient catalysts. Recently, the influence of 'confined space' towards chemical reactions has been of great interest. When the geometry of the reaction space is confined to the micro- or nano-scale, unique physical and chemical traits emerge that are not observed in the bulk dimension. Accordingly, the kinetics, mechanism, or selectivity of various reactions have been reported to differ from the bulk.

For instance, Zare *et al.* [16–19] have reported acceleration of various reactions taking place in microdroplets. In their work, electrospray techniques were used to form droplets containing the reactant, with mass spectroscopy as the method for measuring the reaction rate. Dramatic enhancement of rates of reactions occurring in the microdroplets compared to the bulk were observed, in some cases exhibiting increase rates as high as 10^6 fold [16]. Although the exact reasons for the facilitated reactions in the microdroplets are not yet confirmed, the differing environment in the microdroplet (such as pH, concentration, surface charge, electric field), due to spatial restriction and increased surface-to-volume ratio have been suggested as possible reasons.

Confining the reaction space has also been used as a strategy in enzymes to regulate the pathway of cascade reactions, a term known as 'substrate channelling' [20]. An example of substrate channelling involves the intramolecular tunnel structure observed in tryptophan synthase. This enzyme catalyzes a two-step reaction where indole 3-glycerol-phosphate is converted to indole, which in turn converts to tryptophan. A 2.5 nm long hydrophobic tunnel was discovered to be formed inside the enzyme, spatially separating the intermediate with the bulk phase. This ensures

that the reaction proceeds through a specific pathway, reducing the risk of intermediate diffusion to the bulk, or unwanted side reactions [21]. Inspired by such catalytic approaches of enzymes, some nanoparticle electrocatalysts have been engineered to mimic the geometric features of enzymes in order to enhance catalytic efficiency [22,23].

Confined space of chemical reactions can also be generated by the structure of surrounding catalysts. The reduction reaction of 4-nitrophenol was reported to be enhanced inside hollow, cage-like nanoparticles, a phenomena termed the 'cage effect' [24–26]. Furthermore, the corresponding frequency factors obtained from Arrhenius plots revealed higher values than those reported in the literature, suggesting unique reaction properties due to confinement effects coming from the cavity geometry [25].

1.1.3 Molecular dynamics in confined space

A question arises whether or not the confined space affects electrochemical reactions, and specifically how it is influenced. The first aspect to consider is the molecular dynamics of reactant molecules upon confinement. The diffusion of the molecules in the solution is known to occur through random walk processes. White *et al.* [27] carried out Brownian dynamic simulations based on the random motion of reactant molecules. The simulated trajectory of a molecule enclosed in a spherical solution demonstrated that the random walk motion gave the molecule a chance to explore a small region of space thoroughly before diffusing away. That is, if the reactant molecule is in the vicinity of the electrode, the likelihood of the molecule to interact with the electrode surface multiple times is enhanced. Also, the molecule is

prone towards multiple successive collisions with the surface, due to the close proximity with the surface after the initial collision. The enhanced collision of molecules confined near the electrode surface was further investigated by simulation and voltammetry of redox molecules confined to the electrode through a flexible molecular tether [28].

A case where the confined geometry influences the molecular dynamics can be also found in gas phase reactions occurring at solid, mesoporous catalysts. When the mean free path of molecules is considerably bigger than the pore diameter, Knudsen diffusion is the dominating transport mechanism for gas molecules. In this regime, collisions of the molecules with the pore wall take place more frequently than collisions between the molecules [29,30]. Based on the characteristics of Knudsen diffusion, Debe [31,32] suggested that the surface area distribution of the catalysts would impact the physisorption attempt frequency of oxygen molecules upon the catalyst surface, therefore influencing the rate of chemisorption. Electrodes with extended surface area, such as porous structures with pores sizes in the Knudsen regime, would exhibit higher physisorption frequency with the catalyst surface than dispersed Pt/C electrodes. Such additional catalytic factor originating from the surface spatial distribution was found to be dependent on the inverse of the surface area per unit volume of the catalyst [31].

1.1.4 Electron transfer models and rate formalism based on microscopic theories

From the aforementioned reports, it can be speculated that the molecular motion is altered by the nanoconfined space, consequently affecting its interaction with the electrode surface. However, electron transfer at the electrode surface involve various factors that depend on the characteristic of the reactant as well as surrounding environments. To gain insight on how the confined geometry impact the electron transfer kinetics, it would be helpful to look into the theoretical treatments of electron transfer models and its corresponding kinetic rates.

A representative method of classifying electrochemical reaction mechanisms concerns the spatial position of the reaction site near the interfacial region, and if applicable, the presence of a bridging ligand in the course of the reaction. In the outer sphere pathway, the reactants and the intermediates do not interact with the electrode surface strongly, and do not involve bridging ligands. Thus the electron transfer is thought to occur by electron tunneling through a solvent monolayer between the reactant and the electrode. On the other hand, in the inner sphere pathway, the reactants and intermediates form strong interactions with the electrode surface, and in some cases, involve bridging ligands between the reactant and the electrode. The reactants, intermediates or products involved in this pathway often penetrate the inner layer of solvent molecules that are adjacent to the electrode surface, making direct contact with the surface (**Figure 1-2**). Due to such characteristics, outer sphere pathway reactions are generally less affected by the electrode material, whereas inner sphere reactions are greatly dependent on the intrinsic properties of the material.

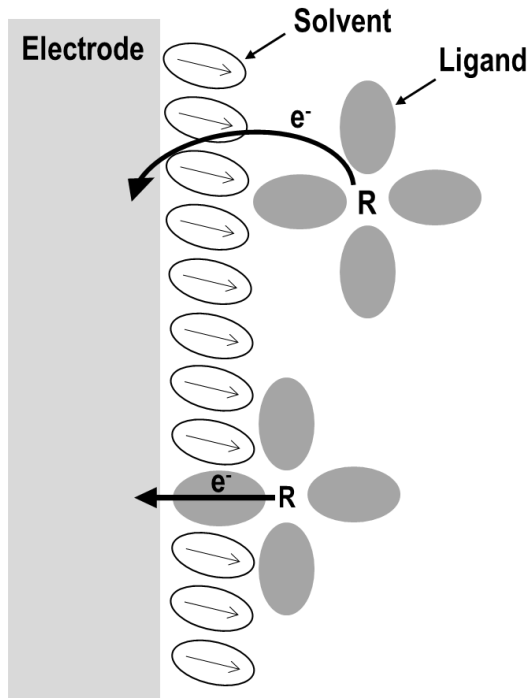

Figure 1-2. Schematic diagram of outer-sphere (upper diagram) and inner-sphere (lower diagram) electron transfer reaction.

Theoretical treatments of outer sphere electron transfer have been developed over the last 50 years [33,34]. For a single electron transfer reaction, we can consider the following:

$$O + e^- \leftrightarrow R \quad (1)$$

where O and R represent the oxidized and reduced forms, respectively.

The electron transfer process consists of the following steps; (a) the reactant molecule locates within close proximity with the electrode surface, forming a

precursor state, (b) formation of transition state, where activation of nuclear reaction coordinates occurs, (c) electron tunneling, (d) nuclear deactivation, forming a successor state, and (e) dissociation of the successor state towards the final product. (**Figure 1-3**)

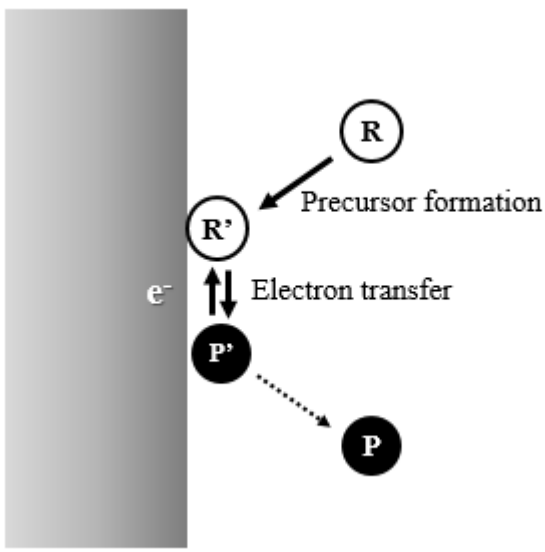

Figure 1-3. Scheme of electron transfer. R and R' represent the reactant and the precursor state, P and P' represent the product and successor state respectively.

The rate constant of the outer sphere electron transfer can be thus expressed as the following:

$$k_f = K_P \nu_n \kappa_{el} \exp(-\Delta G^*/RT) \quad (2)$$

ΔG^* represents the activation free energy for the elementary step of the precursor state, K_P is the equilibrium constant for the formation of precursor state, ν_n is the nuclear frequency factor, and κ_{el} the electronic transmission coefficient.

Two models are considered for the outer-sphere electron transfer process [34]. The 'collisional model' regards the electron transfer reaction to take place through collision between the reactant and the reaction plane (presumably the outer Helmholtz plane) at the electrode surface. This model assumes the pre-exponential factor to include the collision frequency. However, since outer-sphere reactions proceed by electron tunneling, electron transfer is not limited to reactants that collide with the electrode surface, but can also occur for isolated reactant molecules that are close enough to the surface. Thus, the collisional model may underestimate the amount of molecules contributing to the observed reaction.

The 'encounter pre-equilibrium model' views the electron transfer taking place through the activation of the reactant, forming an intermediate precursor state. The activation of reactant molecule is made by solvent-reactant energy transfer, without having to collide with the reaction plane. Thus, electron transfer may take place for reactant molecules that are located within close proximity from the electrode surface. In this case, the observed electron transfer reaction rate will be an integral of local rates, each corresponding to different positions and different values κ_{el} of and ΔG^*.

In this connection, the K_P is expressed as the following:

$$K_P = K_0 \exp(-w_p/RT) \quad (3)$$

$$= \delta r \exp(-w_p/RT) \quad (4)$$

where w_p is the work term for forming the precursor state from the reactant in the bulk solution, and K_0 is a statistical term, which is equal to the effective "reaction zone thickness", δr. It represents the effective thickness region near the electrode where electron transfer take place, and is typically a few Ångstroms.

The inclusion of δr in the rate constant reflects that reactants far from the electrode will barely contribute to the observed rate, as the electron tunneling probability would be low. In this regard, the value of δr is determined by the dependence on the nuclear frequency factor κ_{el} upon the electrode-reactant distance. For non-adiabatic pathways, where there is weak overlap between the reactant and the electrode surface, κ_{el} is less than unity, and can be expressed as the following,

$$\kappa_{el} = \kappa_{el}^0 \exp[-\beta(r-\sigma)] \quad (5)$$

where κ_{el}^0 is the electronic transmission coefficient at the closest approach of reactant and electrode surface (σ), r is the separation distance of reactant and surface, and β is a scaling constant. Thus the combined $\delta r \kappa_{el}^0$ represent the 'effective' electron tunneling distance.

From the microscopic theories of outer sphere pathways, it can be conjectured that for reactants with weak interaction with the surface, the spatial proximity of the reactant to the electrode surface is crucial, and even in the closest approach, there is

a chance that electron transfer may not take place (owing to κ_{el}^{0}<1). Therefore, it must go through multiple attempts for electron transfer to take place.

Theoretical consideration of inner sphere pathways, on the other hand, is much more complicated, as reaction pathways are exceedingly sensitive towards the crystalline facets, as well as special sites (such as steps, terraces) of the catalyst surface. The first step of inner sphere electron transfer mechanisms are generally assumed to be dissociative or non-dissociative adsorption of the reactant molecule on the electrode surface. Oxygen reduction reaction (ORR) is a representative reaction which goes through the inner sphere pathway. ORR on platinum surfaces has been generally known to proceed through the following mechanism (**Figure 1-4**) [35,36]. The rate determining step has been acknowledged to be strongly related to the adsorption energy of intermediate species (OOH^{*} or OH^{*}). Therefore, for catalyst development involving inner sphere reactions, much effort has been made to adjust the adsorption energy of the catalyst surface [2–5].

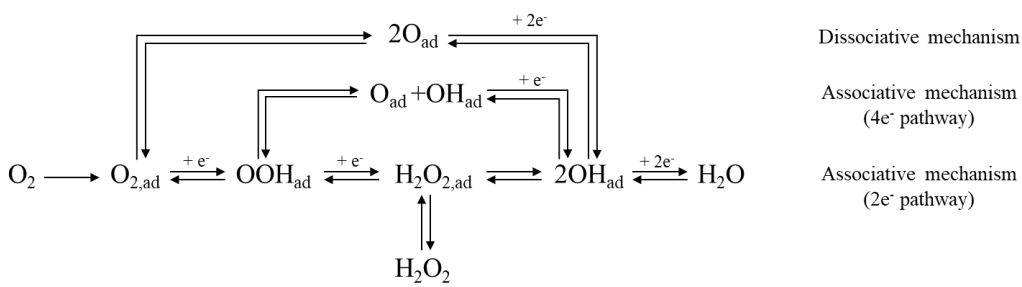

Figure 1-4 Dissociative and associative Oxygen reduction pathways.

1.2 Effect of confined space in electrochemistry

1.2.1 Electrochemical confinement effects

As spatial proximity between reactants and the electrode surface is crucial to electron transfer, especially for reactions that proceed through weak- or non-adsorptive pathways. Reactant molecules placed in confined geometry, for example, inside the nanopores of nanoporous electrodes, are spatially confined to the vicinity of the electrode, as their distances from the inner electrode surface should be smaller than the nanopore radius. The reactant molecule is far more likely be in the vicinity of the electrode surface again even after wandering off, as the inner electrode walls are merely several nanometers apart. Thus, reactant molecules in the nanoporous electrode would reside within the reaction zone more frequently, resulting in higher chances to undergo electron transfer (**Figure 1-5**). This scheme of facilitated electrochemical reaction has been used to account for electrokinetic enhancements in nanoporous electrodes [37–39].

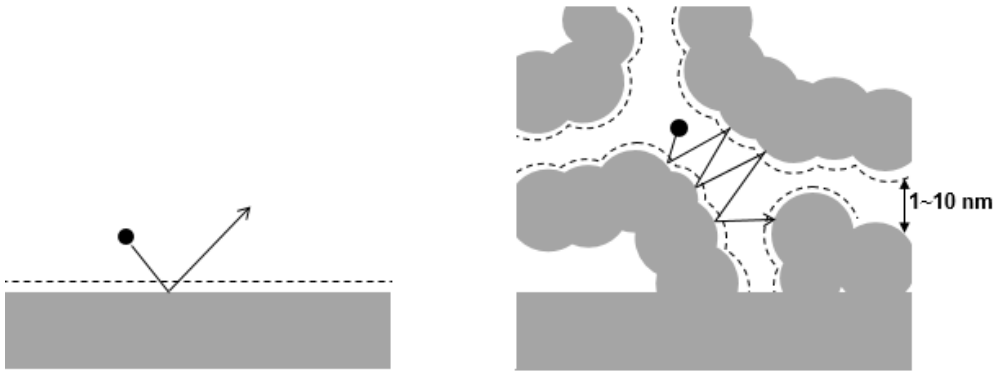

Figure 1-5. A simplified trajectory of a reactant molecule (expressed as a circle) near the surfaces of planar (left) and nanoporous (right) electrode. The dashed line near the electrode surface represents the approximate boundary of the reaction zone. The arrows exemplify a simplified trajectory of the reactant molecule.

Confined geometry of electrodes may also alter the electrocatalytic environment that affect electron transfer process in other ways than molecular dynamics. Variation of solvent properties upon confinement inside solid nanopores have been extensively investigated, theoretically and experimentally [40–44]. In the earlier studies using molecular dynamic simulations, water molecules spatially confined in spherical cavity were calculated to have smaller dielectric constant values than those of the bulk [40]. More recent simulation studies showed reduced dielectric constants of water molecules placed between narrow slab geometries under an external electric field, and demonstrated further reduce of dielectric constants upon narrowing gaps [43]. Recently, dielectric constants of water confined in slit-like channels were experimentally observed with varied heights of the channel [44]. The diminished dielectric constants of solvents upon confinement were attributed to the thin solvent

layer near the nanochannel surface (near-surface layers), which have exceedingly low dielectric constants.

Solvation processes of solvent molecules upon confinement were also reported to differ from those of the bulk [41,45]. For example, rotation and solvation dynamics of the solvent molecules upon confinement were observed using fluorescent Coumarin 153 dyes in sol-gel glasses with pore sizes 25 Å and 50 Å in average. The rotation dynamics and solvation process of the ethanol solvent appeared to be slowed down with the decreasing pore sizes of sol-gel glasses [41].

Pore sizes of few nanometers or below have been reported to affect the adsorption properties of confined molecules. For example, reactant molecules confined in the gap between platinum nanoparticle encapsulated by hexagonal boron nitride (h-BN) layer was investigated. The electronic interaction between h-BN with the platinum nanoparticle surface cause weakening adsorption of the reactant molecules towards the platinum surface, leading to enhanced electrochemical rates [46]. In other works, DFT calculations of molecules confined between closely positioned metal surfaces demonstrated that molecular properties including bond length, dissociation energy barriers, and adsorption energies could be altered as a result of confinement [47].

1.2.2 Nanoconfinement effects in nanoporous electrodes

Nanoconfinement effects in electrochemistry have been actively investigated using nanoporous electrodes, with pore sizes that are typically on the range from 2 to several tens of nanometers. Earlier works have reported uniquely enhanced electrocatalytic effects towards oxygen reduction [48], hydrogen peroxide [9], or glucose [49] with mesoporous platinum electrodes compared to planar electrodes. Han *et al.* [37] compared surface area normalized current densities of hydrogen peroxide reduction using nanoporous Pt and flat Pt, and attributed the additional catalytic factor to the confinement effects. Grand canonical Monte Carlo simulations of simplified porous geometries were also performed, which predicted that nanoconfinement effects would be more prominent for slow, non-adsorbing reactions. The effect of reactant adsorption upon the nanoconfinement phenomena was further experimentally investigated by comparing the electrooxidation reactions of two isomers 1-butanol and 2-butanol, which differ in reaction mechanisms. By comparing oxidation reactions using nanoporous Pt and flat Pt, only the non-adsorptive oxidation of 2-butanol showed enhanced current density for the nanoporous electrode [39].

Comparing catalysts with similar surface characteristics with differing structures would be helpful in ruling out catalytic effects originating from the nanostructure surfaces. Snyder *et al.* [50] measured the oxygen reduction kinetics with varying sizes of nanoporous Nickel/Platinum (Ni/Pt) alloy nanoparticles. The nanoparticles with nanoporous geometry exhibited enhanced specific activity than nonporous, solid Ni/Pt nanoparticles despite their similar Ni content. More recently, nanostructured platinum electrodes with differing structures were compared [51]. Nanoporous platinum electrodes (L_2-ePt) used in this work were obtained by

depositing Pt nanoparticles on planar Pt substrates. Regulation of the deposition time allowed fabrication of a thin Pt nanoparticle layer, absent of pore structures. By comparing the electrocatalytic activity of thin nanoporous Pt with thicker nanoporous Pt electrodes, catalytic effects arising from the nanoporous structure could be observed, while ruling out catalytic effects from the roughened surface (e.g. crystalline facets).

Investigation of the confined electrode structures upon electrochemical reactions have been carried out using electrodes with well-defined nanostructures, such as nanocages. Nazemi *et al.*[52] examined the electrochemical nitrogen reduction rate using hollow Au nanocages and solid Au nanocubes, nanospheres, and nanorods. The best ammonia yield and faradaic efficiency were observed for the hollow Au nanocages, owing to confinement of reactant intermediates inside the cavity.

1.2.3 Challenges in experimental studies of nanoconfinement effects

Previous studies in nanoconfinement effects have mostly relied on nanoporous electrodes fabricated by noble metals such as platinum or gold. However, as noble metals have surfaces with high intrinsic catalytic activities, more so when fabricated into nanoporous structures, catalytic effects purely from the geometrical factor is difficult to observe. Nanostructuring electrodes lead to increase of defects or altered crystalline facets of the surface, which may appear as additional catalytic effects. Also, platinum and gold possess highly adsorptive surfaces which can interfere the catalytic pathway.

Furthermore, in most studies, electrocatalytic performances were observed for proton-coupled, multi-electron transfer reactions such as oxygen reduction, hydrogen peroxide reduction, or glucose oxidation. This complicates the clear observation of electrokinetic phenomena, as the reaction is composed of multisteps involving various intermediates. Also, the proton depletion inside the nanopores could interfere with the reaction kinetics.

Therefore, an alternative strategy is needed in which the catalytic effect from the morphology of the nanoporous electrode can be isolated. In this context, we implemented a new strategy in observing nanoconfinement effects in nanoporous electrodes. First, a low catalytic material, Indium tin oxide (ITO) was used as the nanoporous electrodes. Simple, one electron transfer reaction of $Fe^{2+/3+}$ was chosen as the electrochemical reaction under study. The electron transfer kinetics were observed by tuning the nanoporous thickness, thereby effectively eliminating the catalytic activity from the nanoporous surface.

Chapter 2.

Investigation of Nanoconfinement effects at Nanoporous Indium Tin Oxide Electrodes

2.1 Introduction

Nanoporous structured electrodes have attracted significant interest as efficient electrocatalysts owing to its catalytic effects arising from their nanoscale geometry. Various applications of nanoporous electrodes have been reported, ranging widely from energy conversion and storage systems, electrochemical sensors, and neural probes. Previous studies have reported facilitated proton transfer as well as electron transfer (ET) kinetics of the nanopores [37,53]. The remarkable electrocatalytic effects of nanoporous electrodes have been commonly explained on the basis of enlarged surface area [54], crystalline facet [55], and surface defects [12], all of which are associated to the characteristics of electrode surface and mostly on the premise of adsorptive reaction mechanism.

Notwithstanding the conventional, adsorption-based research for electrocatalyst designs, non-adsorptive mechanisms may also play a significant role in the catalytic enhancement. One of the probable factors in nanoporous electrodes is the geometric effect of the confined space, which is formed by the surrounding electrode surfaces on a nanoscale. A probable mechanism is the augmentation of the collision frequency between the reactant and the electrode surface [37,39], while other factors such as the electronic structure of reactant molecules [47] and solvent properties [42] in the nanopores should be considered as well. Yet the exact origin of non-adsorptive mechanism based electrocatalysis at nanoporous electrodes and its actual contribution towards the electrocatalytic performance remain unexplored.

This may be largely due to the difficulties in quantitatively evaluating the electrocatalytic activity of nanoporous electrodes. The measured faradaic current of nanoporous electrodes increases with the electrochemically active surface area (ECSA) of the electrode. Thus, in order to acquire effective faradaic rates of given

nanoporous electrodes, the current density, obtained by normalizing the current with the real surface area of the electrode, should be measured. For a fair comparison in terms of electrocatalytic activity, it is necessary to assume the entire surface of the nanoporous electrode to participate in the faradaic reaction. However, this assumption fails under mass transfer limiting conditions. Depletion of electroactive species in the deep nanopores occur for fast heterogeneous redox processes [56], leading to inaccurate standard rate constant (k^0) values [57,58]. In terms of investigating nanoporous electrodes, this limits the choice of electrode materials. For example, platinum (Pt) surface itself show intrinsically high catalytic activity for most faradaic reactions, more so when the surface is roughened in nanoporous Pt electrodes. Therefore, for such electrodes, it is difficult to extract the catalytic enhancement arising solely from the geometrical effect of the nanopores. Gold (Au) surface is generally less catalytic than Pt, but most electron transfer reactions occur too fast to investigate electrokinetic studies regarding the geometric morphology. Recently, reduction kinetics of Fe^{3+} at nanoporous Au electrode was quantitatively measured by implementing scanning electrochemical microscope (SECM) [59], which provided a sufficiently fast mass-transfer rate to determine large k^0. Reportedly, the k^0 values obtained at the nanoporous Au were 3 – 5 higher than those measured at flat Au electrode. The basal plane of graphite, a chemically inert surface with sluggish kinetics for most electrochemical reactions, could be an appropriate material in studying the geometrical effects of the electrode. However, in our knowledge, there is no known method to prepare nanoporous electrodes with surfaces of basal plane. In fact, even if nanoporous graphite were prepared, it could not have such basal planes due to its nanoscale curvature. Although other kinds of carbon materials could be attempted, the measured ET rate would be poorly reliable because of the unpredictable distribution of surface functional groups that affect

electrochemical reactions [60,61], and its vulnerability to adsorption of organic impurities [62].

From previous cases of experimental efforts to study the geometric effect of nanoporous electrodes, it can be expected that a moderately slow one-electron transfer reaction without coupled chemical reactions (such as proton transfer), would enable us to clearly observe the influence of nanoporous morphology towards the ET kinetics. On one hand, if the electrode material is chemically inert and weakly adsorptive, it could make the ET reaction appropriately slow. This stimulated us to consider indium tin oxide (ITO) as the material for nanoporous electrodes in studying nano-confinement effects. ITOs have been known to have lower intrinsic electrocatalytic activities than most metals and carbon electrodes, providing a wide potential window and reproducible background currents [63,64]. For these reasons ITOs are commonly used as substrates for electrochemical sensors rather than as electrocatalysts.

In this work, we examine the one electron transfer kinetics of $Fe^{2+/3+}$ in nanoporous ITO electrodes. To eliminate the catalytic activity factor emerging from surface defects of ITO nanoparticles, we compare the electrochemical behaviors of ITO electrodes as a function of the nanoporous layer thickness. We observe clearly the contribution of the nanoporous geometry towards the electrochemical enhancement, and suggest explanations based on a non-adsorption mechanism.

2.2 Experimental

2.2.1 Reagents

Potassium sulfate (≥99.0 %, Reagent plus), Iron(II) sulfate heptahydrate (≥99.0%, ACS reagent), Iron(III) sulfate hydrate (97%), Acetic Acid (≥99.7%, ACS reagent), Hexaaammineruthenium(II) chloride (99.9%, trace metals basis), Potassium chloride (≥99.0 %, Reagent plus) were purchased from Sigma-Aldrich (St. Louis, MO), Ethanol (ACS, ISO, Reag. Ph Eur) was purchased from Merck Millipore, Sulfuric acid (95%) was purchased from Daejung, all of which were used without further purification. All aqueous solutions in this experiment were prepared with ultrapure deionized water (resistivity ~ 18.2 MΩ) produced by NANOpure (Barnstead). ITO nanoparticle powder was purchased from Lihochem, and FTO (Fluorine doped tin oxide) substrates were purchased from Techinstro.

2.2.2 Fabrication and Characterization of nanoporous Indium Tin Oxide electrodes with various thicknesses

Nanoporous ITO electrodes were fabricated from modification of a previously reported method [65]. First, the ITO nanoparticles were repeatedly washed in acetone and ethanol several times and dispersed in 5 M acetic acid / ethanol solution. The flat ITO and FTO substrates were washed by sonication in acetone, isopropanol

and water each for 20 min, followed by air plasma to completely remove residual impurities.

ITO nanoparticles (30~40 nm diameters) were dispersed thoroughly in 5 M acetic acid / ethanol by sonication, then deposited on FTO substrates by spin coating. In order to acquire smooth nanoporous layered films, we took the supernatant liquid of the ITO nanoparticle slurry (gained after a short centrifuge process) as the spin coating solution. FTO was chosen as the substrate for the deposition of nanoporous ITO layers due to its good thermal stability and low background catalytic activity [66]. The thicknesses of the nanoporous layer of ITO electrodes were tuned by increasing the number of repeated spin coating processes, where the spin coated substrates were dried on a hot plate at 100 ℃ for 10 min between each process. Afterwards, the nanoporous ITO films were annealed in two steps; first at 500 ℃ in atmospheric air for 1 h, and then at 300 ℃ in forming gas (5% H_2 / Argon gas) for 1 h to raise the conductivity of the ITO films [67,68]. The heating process was done with a tube furnace [Thermal CVD System, SciEnTech]. For the electrochemical experimnets, the electrical contact was made by attaching aluminum conductive tape near the edge of the FTO substrate where spin coating had been prevented by Kapton tape. Then a portion of the nanoporous ITO surface (5 mm diameter) was selectively exposed by using an electroplating tape (3M™ Electroplating Tape 470). The electrodes were tested after carefully rinsing the surface with deionized water.

The morphology of the fabricated nanoporous ITO films was observed by Focused Ion Beam equipped with a Field-Emission Scanning Electron Microscope (Helios 650, FEI, USA).

2.2.3 Electrochemical Methods

The electrochemical setup for all experiments in this study was a three electrode system with an Hg/Hg_2SO_4 (saturated K_2SO_4, RE-2C, BAS, Inc.) or Ag/AgCl (3 M NaCl) as the reference electrode, and Pt mesh as the counter electrode. Cyclic voltammetry was performed by a commercialized potentiostat (Model CHI604, CH Instruments). The instrument for electrochemical impedance spectroscopy (EIS) was a Reference 600 equipped with EIS300 electrochemical impedance spectroscopy software (Gamry Instruments) over a frequency range from 10 kHz to 0.1 Hz, with a programmed AC input of 10 mV amplitude superimposed on the DC offset potential. EIS measurements were done in 10 mM $Fe(II)SO_4$ + 5 mM $Fe(III)_2(SO_4)_3$ / 100 mM H_2SO_4 / 500 mM K_2SO_4. The DC potential used for EIS was determined by the mean of the redox peak potentials of the cyclic voltammogram. Temperature environments were tuned by an ethanol circulation bath (WCR-P8, Daihan Scientific) with a water jacketed cell.

2.3 Results and Discussion

2.3.1 Characterization of nanoporous Indium Tin Oxide electrodes

The FESEM (field emission scanning electron microscope) images (**Figure 2-1**) shows the morphologies of the fabricated nanoporous ITO films. The cross sections of the films reveal that the electrodes have porous structures with random pores formed by the accumulation of ITO nanoparticles. The pore size ranges from several tens to a hundred nanometers. The thickness of nanoporous films spin coated 2, 3, 4 and 6 times are measured from the cross section SEM images, and are approximately 281, 463, 638, 962 nm respectively (The electrode spin coated only once had sparse ITO nanoparticles distributed on the surface, making it difficult to determine the exact thickness.) This indicates that the nanoporous layer thickness increased regularly (~170 nm) per each spin coating process. Thus, each deposited nanoparticle ITO layer is piled up on top of the pre-deposited layer, where the repetition of the deposition simply adds the same porous layers, thus retaining the average pore sizes, density of surface defects, etc. For convenience, we will designate the nanoporous ITO electrodes 'ITO x*n*', where *n* represents the number of the spin coating processes. Higher *n* obviously indicates thicker nanoporous ITO layers.

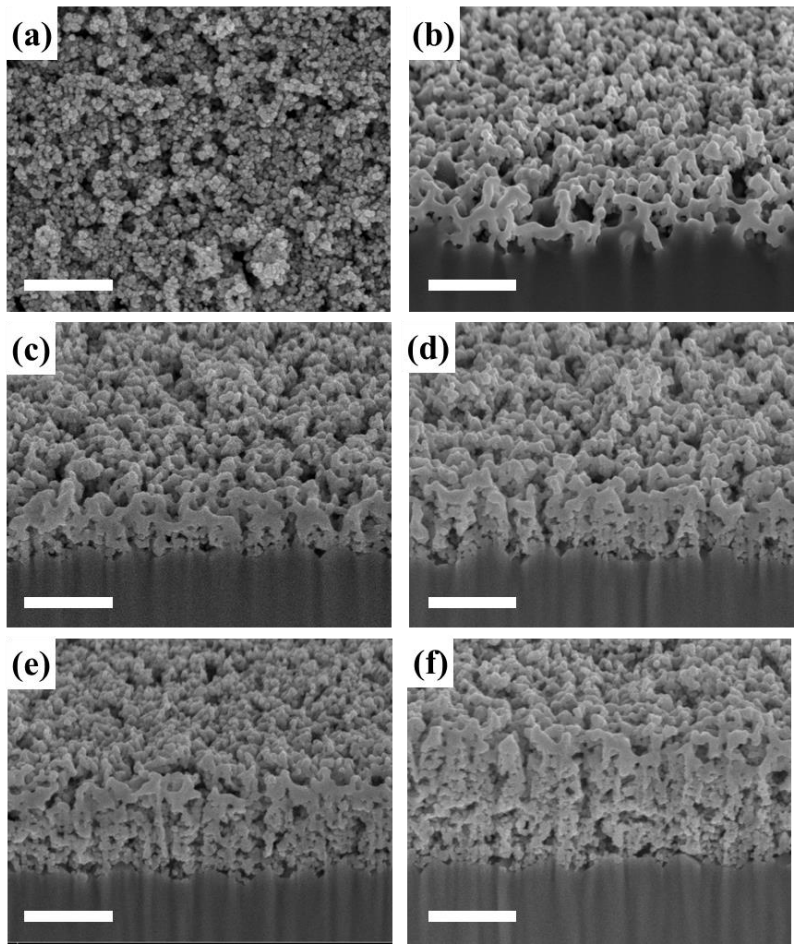

Figure 2-1. (a) Top view Field-Emission Scanning Electron Microscope (FESEM) image of nanoporous ITO electrode spin coated 3 times. Figures (b-e) represent the cross section FESEM images of electrodes spin coated (b) once, (c) 2 times, (d) 3 times, (e) 4 times, and (f) 6 times. The scale bar in each image represent 500 nm.

Cyclic voltammetry for a well-known reversible redox reaction of 1 mM $Ru(NH_3)_6^{3+}$ / 1 M KCl reveals information regarding the conductivity of the nanoporous ITO layers (**Figure 2-2**). As expected, the peak-to-peak separation is unchanged regardless of the electrode thickness, and the voltammograms are not inclined, indicating sufficient conductivity of the fabricated nanoporous ITO films to be utilized as electrodes.

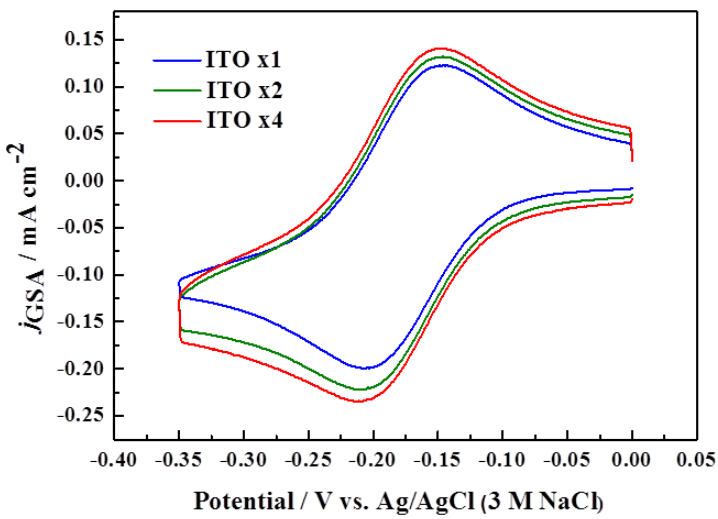

Figure 2-2. Cyclic voltammogram of various nanoporous ITO electrodes measured in 1 mM $Ru(NH_3)_6^{3+}$ / 1 M KCl. The current density in the y-axis is the measured current divided by the geometric surface area of the electrode. Scan rate 50 mV/s.

2.3.2 Measurements of $Fe^{2+/3+}$ electrokinetics at nanoporous ITO electrodes

In order to observe the enhancement of faradaic current density coming from the confinement in nanopores, we selected $Fe^{2+/3+}$ as the redox couple since it involves a single electron transfer without any coupled chemical reactions. Such a simple electrochemical reaction would offer us a straightforward model that enables us to confirm the nano-confinement effect and assess the significance of the faradaic enhancement for a given sluggish process.

First, cyclic voltammetry was carried out with nanoporous ITO electrodes of various thicknesses, and the results are shown in **Figure 2-3**. Both the anodic and cathodic peaks shift consistently, leading to smaller peak-to-peak potentials as the electrode thickness increases. While this may suggest enhancement of electron transfer due to thicker nanoporous layers, the catalytic contribution from the nanoporous geometry cannot be confirmed with this result alone, since cyclic voltammetry is measured in a wide potential range with high overpotentials, where the mass transport effects interfere as well [69].

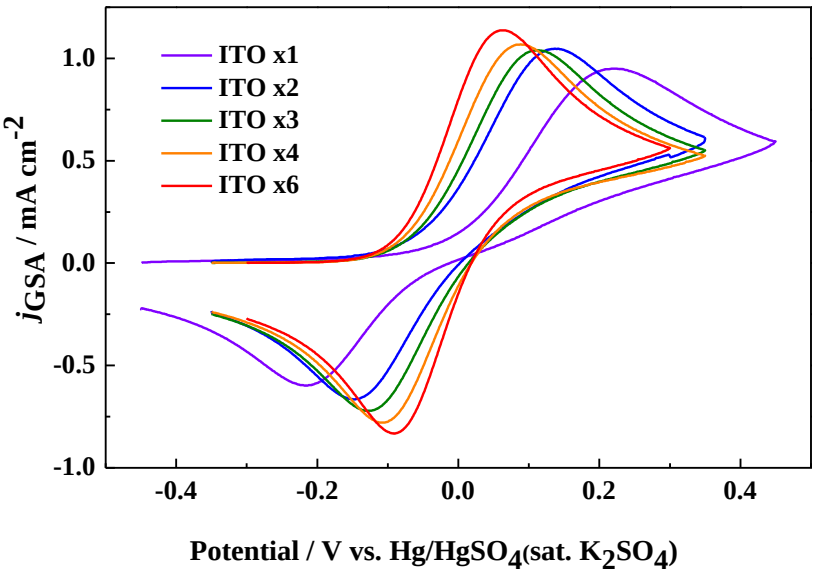

Figure 2-3. Cyclic voltammograms of ITO x1, ITOx2, ITO x3, ITO x4 and ITO x6 electrodes measured in 10 mM Fe(II)SO_4 / 100 mM H_2SO_4 / 500 mM K_2SO_4 solution, where the current density in the y-axis is the current divided by the geometric surface area of the electrode. The scan rate is 50 mV/s.

Thus, a quantitative evaluation of the electrokinetic enhancements, with minimal influence from factors other than the heterogeneous electron transfer kinetics, is required in order to observe the electrocatalytic effects in the nanoporous ITO electrodes clearly. The most common method for extracting kinetic parameters in electrochemistry is the Tafel plot, where the kinetic parameters are evaluated by measuring currents at relatively large overpotentials. However, electron transfer reactions occurring at thick ITO nanoporous layers are likely to reach the mass transfer limit even at moderate overpotentials, especially in the deep regions of the nanoporous films [70]. This would lead to deviation from linearity at most

overpotential regions. The limitation due to mass transfer could be overcome by methods involving forced convection, for instance using Rotating disk electrode (RDE). However, there are some practical difficulties in conducting electrochemical experiments with the nanoporous ITO electrodes in the RDE system. For instance, as the FTO beneath the ITO porous layer is coated on a glass substrate, the fabricated ITO electrodes are only conductive on the upper side. This makes the ITO electrodes difficult to be imbedded in the RDE shaft with ensured electric connection. Direct deposition of ITO nanoparticles directly on disk electrodes would be problematic, because the fabrication of nanoporous ITO electrode requires high temperature annealing (up to 500 ℃).

Rather than employing electrochemical methods that apply large overpotentials, which would give rise to reactant depletion in nanopores, measuring electron transfer kinetics near the equilibrium potential with small overpotential would enable us to observe the electrocatalytic process with minimal interference from mass transfer. This approach was made by using electrochemical impedance spectroscopy (EIS). As EIS is measured near the equilibrium potential with a small alternating signal applied (usually 5~10 mV), in the presence of both redox species in the solution, it allows us to investigate electron transfer kinetics electrode surface under the condition free of mass transport. Thus by using EIS, we can obtain the electrochemical rate constants under the kinetic controlled region, even in the absence of forced convection.

The experimental EIS data can be analyzed by fitting with the Randles equivalent circuit [71,72] shown in **Figure 2-4 (a)**. In this study, the double layer capacitance element in the Randles circuit was replaced by a constant phase element (CPE) to account for non-ideal capacitance behaviors [73,74]. An example showing EIS fitting result is shown in **Figure 2-4 (b)**, and the values obtained from the fitting process are summarized in **Table 2-1**. The R_{ct} and R_u values represent the charge

transfer resistance and the uncompensated resistance, respectively. The Q and α represent the parameters related to the CPE component, where CPE approach the ideal capacitor as α becomes closer to 1.

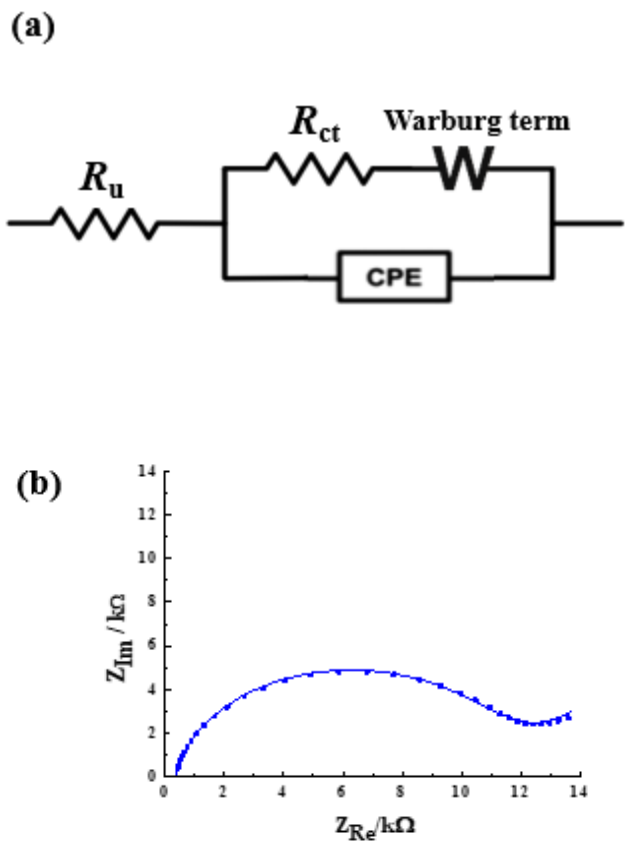

Figure 2-4. (a) Randles equivalent circuit that was used in fitting the EIS results. (b) An example of EIS fitting result with the equivalent circuit shown in (a), using the EIS data of ITO x2 electrode measured in 10 mM Fe(II)SO_4 + 5 mM Fe(III) SO_4 / 100 mM H_2SO_4 / 500 mM K_2SO_4.

Parameters	R_{ct} [ohm]	R_u [ohm]	Q [s^{α}/ohm]	α	W_d [$s^{1/2}$/ohm]
EIS fitting results of ITO x2 electrode	517.5	17.09	7.985E-05	0.9021	7.151E-03

Table 2-1. Parameter values obtained from the fitting process shown in **Figure 2-4 (b)** are summarized.

Finally, the Warburg term in the equivalent circuit indicates the resistance at low frequencies below 1 Hz that appear due to mass transfer. From the values extracted from EIS fitting, we can obtain two important parameters related to the electrode kinetics – the effective capacitance of the electrode, and the standard rate constant of the redox couple $Fe^{2+/3+}$.

By applying the EIS fitting results into the Brug equation [72,74], we can extract the effective interfacial capacitance value C_{eff}

$$C_{eff} = Q^{1/\alpha} \left(\frac{R_u R_{ct}}{R_u + R_{ct}}\right)^{(1-\alpha)/\alpha} \quad (1)$$

The current density measured at nanoporous electrodes need to be corrected by the real surface area of the electrode in order to obtain rate constants where the increased faradaic current due to the enlarged electrode area is excluded. The capacitance value acquired from equation (1) can be used to evaluate the effective surface area of the electrode. To verify the correlation between the effective surface area of the electrode and the interfacial capacitance calculated from EIS fitting, we also compared the capacitance values with the charging current values measured by cyclic voltammetry in the absence of the redox species $Fe^{2+/3+}$ (**Figure 2-5** and **Table 2-2**). The cross check between the two methods show that the relative charging current from cyclic

voltammetry proportionally correlates with the interfacial capacitance from EIS. Thus, the 'roughness factor', which is defined as the ratio of the nanoporous surface area to that of flat electrode, can be obtained by the capacitance values of the ITO electrodes divided by those of the bare ITO electrode. Assuming that the real surface area of bare ITO electrode approximately equals its geometric area, the roughness factor is used throughout the paper to correct the kinetic data from the nanoporous electrodes with regard to their real surface area.

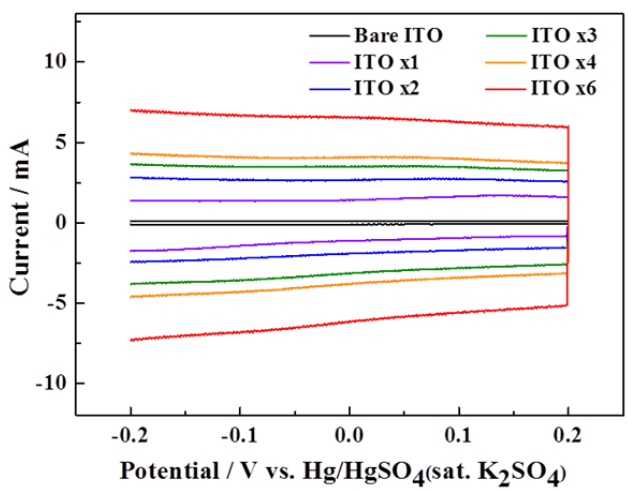

Figure 2-5. The charging current of nanoporous ITO electrodes obtained by cyclic voltammetry in the absence of the redox species $Fe^{2+/3+}$ (100 mM H_2SO_4 / 500 mM K_2SO_4). The scan rate is 50 mV/s. The charging current values displayed in **Table 2-2** were obtained by averaging the value of anodic and cathodic charging currents at 0.0 V (vs. $Hg/HgSO_4$, sat K_2SO_4).

Electrode		Bare ITO	ITO x1	ITO x2	ITO x3	ITO x4	ITO x6
Charging current (i_c) from Cyclic Voltammetry	i_c	1.05E-07	1.248E-06	2.292E-06	3.292E-06	3.929E-06	6.360E-06
	$i_{c,rel}$	**1.00**	**11.88**	**21.82**	**31.35**	**37.41**	**60.57**
Capacitance value (C_{eff}) from EIS fitting	C_{eff}	1.88E-06	2.008E-05	3.890E-05	5.671E-05	7.028E-05	1.193E-04
	$C_{eff,rel}$	**1.00**	**10.69**	**20.70**	**30.18**	**37.40**	**63.52**

Table 2-2. The charging current values at 0.0 V (vs. $Hg/HgSO_4$ / sat K_2SO_4) obtained from the voltammogram in **Figure 2-5** and the capacitance values obtained from EIS data measured in 10 mM $Fe(II)SO_4$ + 5 mM Fe(III) SO_4 / 100 mM H_2SO_4 / 500 mM K_2SO_4 are listed, where both methods are based on the same nanoporous ITO electrode. The two methods are compared by obtaining relative charging currents ($i_{c,rel}$) and relative capacitance values ($C_{eff,rel}$), which are calculated by dividing the i_c, C_{eff} values of each x1, x2, x3, x4 and x6 ITO electrodes with those of bare ITO electrode.

The standard rate constants (k^0) of $Fe^{2+/3+}$ can be obtained from the EIS fitting procedure according to the following equations [71].

$$k^0 = i_0 / FAC \quad (2)$$

$$i_0 = RT / FR_{ct} \quad (3)$$

i_0 denotes the exchange current, F is the Faraday constant in C units, R the gas constant, and T the temperature in K units. A and C are the electrode area and reactant concentration, respectively. R_{ct} is the charge transfer resistance obtained from the EIS fitting process. By substituting the real surface area of the electrode (inferred from the roughness factor) in the electrode area (A) term in equation (2), we can calculate standard rate constant values (k^0) which are normalized by the real surface area of the electrodes. By comparing the standard rate constants (k^0) of $Fe^{2+/3+}$ from ITO electrodes with a series of different nanoporous layers, we evaluated the electrocatalytic effects of ITO electrodes as a function of nanoporous layer thickness.

2.3.3 The surface area normalized rate constants of $Fe^{2+/3+}$ at nanoporous ITO electrodes

The electron transfer kinetics of $Fe^{2+/3+}$ at ITO x1, ITO x2, ITO x3 and ITO x4 nanoporous electrodes were investigated using EIS in 10 mM Fe(II)SO_4 + 5 mM Fe(III) SO_4 / 100 mM H_2SO_4 / 500 mM K_2SO_4 solution. The standard rate constants (k^0) of $Fe^{2+/3+}$ reaction calculated by equation 2 and 3 are presented in **Figure 2-6**, where the averaged k^0 values obtained from three samples are shown as error bars. These results demonstrate that the electron transfer kinetics of $Fe^{2+/3+}$ is more

facilitated at thicker nanoporous layers. It should be noted that this behavior is reproducibly observed even though the kinetic data are normalized by the real surface area.

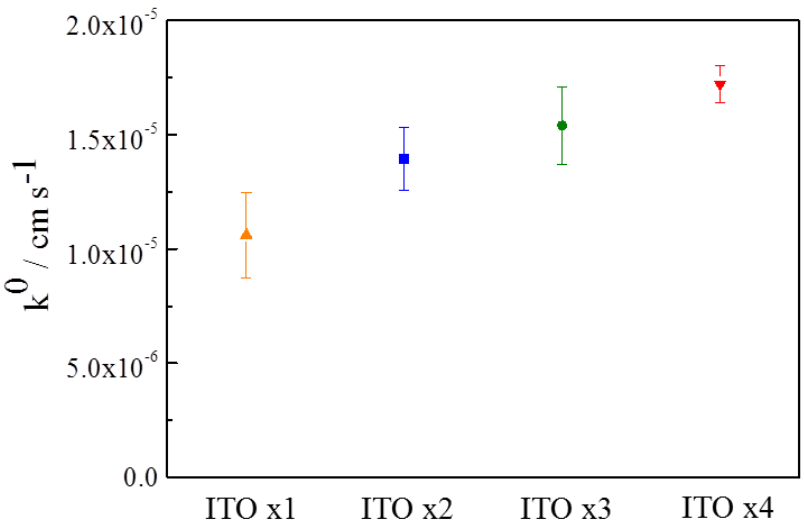

Figure 2-6. The standard rate constant k^0 of the $Fe^{2+/3+}$ reaction from ITO x1 (orange), ITO x2 (blue), ITO x3 (green) and ITO x4 (red) nanoporous electrode, which are calculated from equation 2 and 3. The average k^0 values and the respective standard errors were obtained from three different electrodes made with the same number of spin coating process.

As described in section 2.3.1, the nanoporous layer thickness increases regularly with the repetitive spin coating processes for ITO x2, x3 and x4. Also, the capacitance values in **Table 2-2** ensure that the effective surface area of the electrodes increases proportionally with the number of spin coating. Thus, the nanoporous ITO electrodes with different nanoporous layer thickness differ in the average lengths of porous channel networks, while retaining the average pore sizes and density of surface defects. The gradually increasing rate constants of nanoporous ITO x2, x3 and x4 electrodes show the faradaic enhancement due to the extended nanoporous structure with minimal contribution from both surface area enlargement and the defects on the ITO surfaces.

Thicker nanoporous layers mean more proportion of deeper pores, i.e. extended 'confined space', in which a narrow space in the nanoscale is formed by the surrounding inner surface of the electrodes. The enhanced electron transfer kinetics due to the confined space of nanoporous electrodes have been previously reported, so called 'nanoconfinement effect' [38]. Reactant molecules in the nanopores are confined to areas near the inner electrode surface, leading to higher probability of collisions between the reactant and the electrode surface [27,28]. The augmented collision frequency between the reactant and the electrode surface may eventually result in the enhancement of the electron transfer rate. The nanoconfinement effect have been reported to be particularly noticeable in slow and non-adsorptive faradaic reactions that require numerous collisions with the electrode surface before succeeding in heterogeneous electron transfer [37,39]. Therefore, ITO is an advantageous electrode material in observing the nanoconfinement effect, as it enables augmentation of faradaic current density with less reliance on surface properties affecting adsorptive catalytic processes, such as chemical defects or crystalline facets.

However, as shown in the scheme of **Figure 2-7**, the entire region of the nanoporous structure cannot equally contribute to the nanoconfinement effect. Nanoconfined space can be formed when a certain degree of nanoparticle accumulation has been made. The shallow, non-confined regions of the nanopores that are close to the solution have less chance in confining the reactants, so the reactant molecules are more likely to escape to the bulk solution before succeeding in electron transfer. On the other hand, most of the reactants in the deep, confined regions inside the nanoporous film would actively participate in the nanoconfinement effects. As the nanoporous layer thickness is increased, the proportion of the confined space relative to the non-confined space rises, thus accounting for the kinetic rate enhancement with the thickening porous layer.

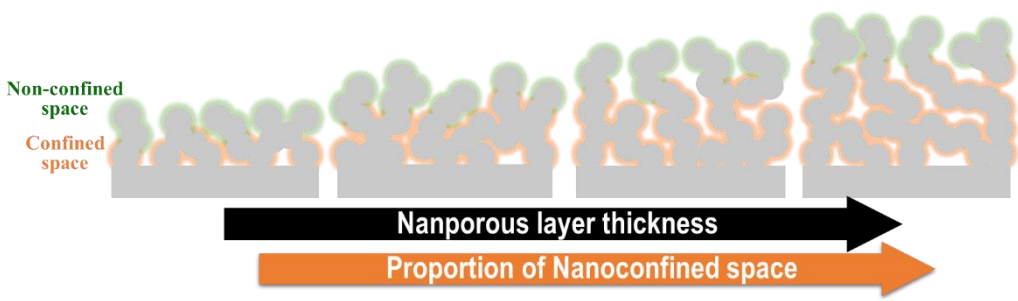

Figure 2-7. Scheme illustrating the increasing proportion of 'confined space' with respect to 'non-confined space' as the nanoporous layer thickness increases.

2.3.4 Nanoconfinement effects as a function of temperature

Further intriguing observations could be made by investigating the nanoconfinement effects according to the temperature environment. The k^0 values obtained from the EIS data recorded at temperature 5, 12.5, 20, and 27.5 ℃ are presented in **Figure 2-8 (a)**. As in the previous section, the surface area normalized rate constants of ITO x1, x2, x3, and x4 electrodes increase with the thickness of nanoporous layers in this range of temperature. Interestingly, the relative enhancements of the k^0 values as a function of film thickness are not constant, but depend on the temperature. For a detailed examination, we set the k^0 values at the thinnest nanoporous electrode (ITO x1) to be unity for all temperatures, and plotted the relative k^0 values, i.e. ratios, of the thicker ITO x2, x3, x4 and ITO x6 nanoporous electrodes against the electrode thicknesses (**Figure 2-8 (b)**). From **Figure 2-8**, we can observe two interesting results.

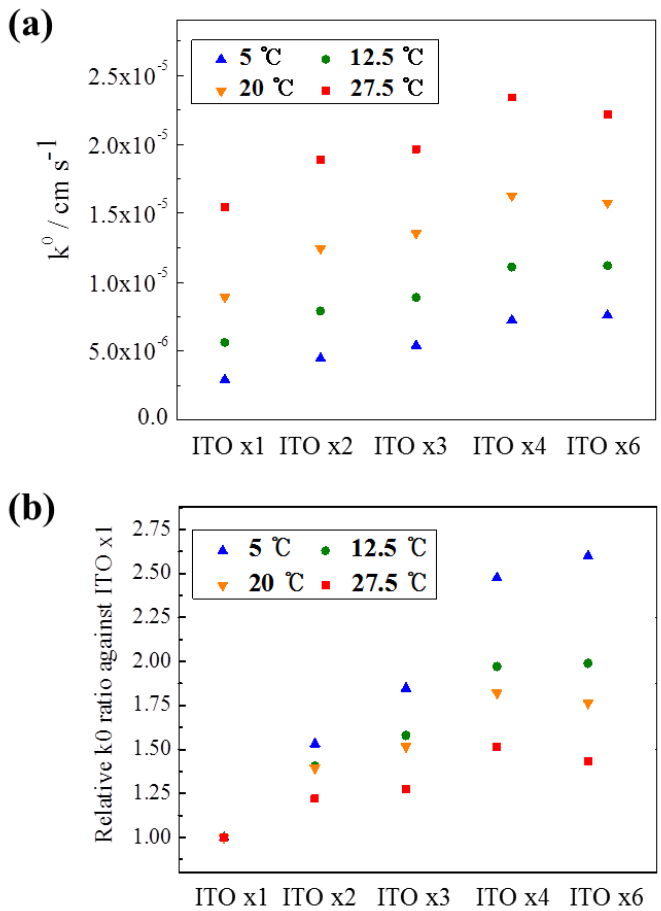

Figure 2-8. (a) The standard rate constants (k^0) of ITO x1, ITO x2, ITO x3, ITO x4 and ITO x6 nanoporous electrodes at 5 ℃ (blue), 12.5 ℃ (green), 20 ℃ (orange), and 27.5 ℃ (red) . The k^0 values are calculated from the EIS data using the equations 2 and 3. All k^0 values are normalized with respect to the roughness factor of the electrode. (b) Setting the k^0 of the thinnest nanoporous electrode (ITO x1) to be unity for all temperatures, the relative ratio of k^0 at thicker nanoporous electrodes (ITO x2, ITO x3 ITO x4 and ITO x6) is calculated and plotted.

The first is the saturation of nanoconfinement effect that occur at excessively thick nanoporous electrodes. If the nanoporous ITO electrode is excessively thick, as in the ITO x6 electrode, addition of confined space would not lead to noticeable increase in overall kinetics, hence the surface area normalized kinetic constants of ITO x6 electrode would show similar values to ITO x4 electrode. Also, the increased kinetic rate constant may lead to depletion of reactant molecules inside the deep nanopores, resulting in relatively lower kinetic constants when normalized by the real surface area. This is demonstrated **Figure 2-8 (a)**, where the surface area normalized kinetic constants continually increase throughout the ITO x1~ ITO x4 electrodes, but remain similar or even decline at the ITO x6 electrode.

The second is the temperature dependence of the degree of kinetic enhancements. The k^0 value as a function of nanoporous layer thickness increases more steeply as the temperature is lowered, as can be seen clearly in **Figure 2-8 (b)**. This is in accordance with previous simulation results [37] which predicted that for slower reactions, the nanoconfinement effect makes more contribution to the apparent faradaic enhancement. As the temperature rises, the probability of electron transfer at the event of collision between the reactant and the electrode surface increases, as inferred from the Arrhenius relationship. Hence, the heterogeneous electron transfer at higher temperatures would require less interaction between the reactant and the electrode surface in order for the electron transfer to take place successfully. Also, though not in the same extent, the collision frequency itself rises with the temperature. The collaboration of these two effects leads to less contribution of nanoconfinement to the overall electron transfer rate at higher temperatures. It is also worth noting that the saturation of nanoconfinement effects that appear when the electrode thickness is increased from ITO x4 to ITO x6 appear more intense at comparatively high temperatures (20, 27.5 ℃ in **Figure 2-8 (b)**) compared to low temperatures (5, 12.5 ℃ in **Figure 2-8 (b)**).

Temperature dependent rate constants were further investigated by Arrhenius plots of ITO x1~ ITO x4 electrodes (**Figure 2-9**). From the Arrhenius plots, it can be seen that the calculated activation energies decrease with the thickening electrodes. Considering that the surface characteristics of electrodes under comparison do not change with the increasing thickness, the gradual decrease of activation energies suggests that the solution environment in which the electron transfer takes place is altered, possibly due to the increased nanoconfined space.

However, changes upon nanopore environment and its influence towards the electrochemical reaction remains unclear. One of the plausible factors affecting the nanopore environment would be solvent properties, as solvent molecules are known to show altered properties upon confinement [40,42,44]. Other factors may include altered electric field inside the nanopores, preconcentration of reactant molecules in the nanopores, stabilization of reactant intermediates, *etc*.

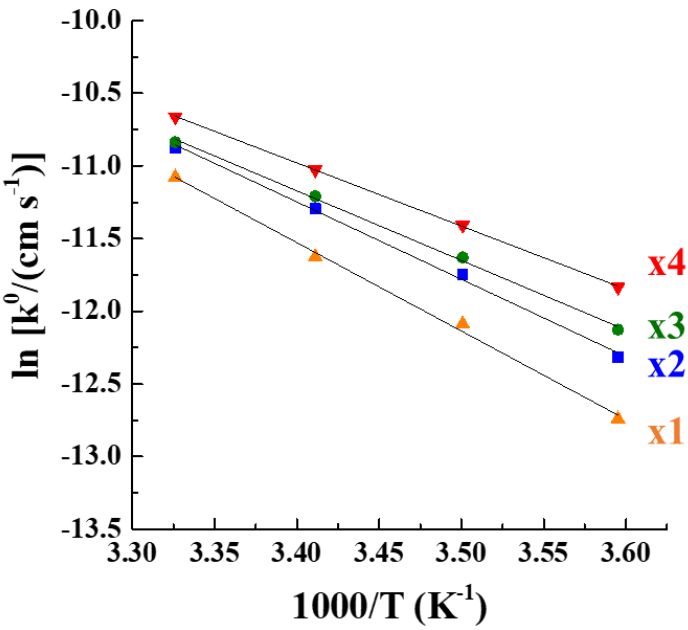

Electrode	x1	x2	x3	x4
E_a [kJ/mol]	50.56	44.21	39.83	36.12

Figure 2-9. Arrhenius plots of x1~x4 nanoporous ITO electrodes (above), and the corresponding activation energies (graph below).

2.4 Conclusion

In this study, we investigated the enhancement of single electron transfer in the absence of coupled chemical reactions using nanoporous ITO electrodes with a series of thicknesses. It was experimentally confirmed that sluggish electron transfer of $Fe^{2+/3+}$ on chemically inert ITO surface is facilitated by the nanoporous morphology of the electrode. The choice of ITO as the electrode material differ from previous studies of nanoconfinement effects, where current densities of electrochemical reactions were observed for nanoporous platinum or gold electrodes. This approach is thus meaningful in observing effects of electrode morphology, free from catalytic contribution from nanostructured novel metal surfaces.

Furthermore, the catalytic activity stemming from the nanostructured ITO surface could be eliminated by depositing ITO nanoparticle layers in series and normalizing each kinetic data with the electrode real surface area. In this way, we were able to maintain the physicochemical properties of nanoporous surfaces such as defects, crystalline facet, and etc., while regulating the proportion of nanoconfined space of the nanoporous electrodes.

Considering the tremendous endeavor for finding better electrocatalysts that are currently focused on the adsorptive processes of reactants involving reactive surface defects, it may be a dilemma to seek active and stable electrocatalysts. In this regard, the geometric enhancement mechanism found at nanoporous structures could be developed as a new strategy for designing future electrocatalysts. In this strategy, collision frequency of the reactant inside the nanopores is the tunable parameter for the electron transfer rate of nonadsorptive processes. This study shows that even ITO, which is well known for its inert surface as an electrode, has the potential of behaving as an electrocatalyst when it is nanoporous. This suggests that we may obtain stable

and reactive electrocatalysts through design and fabrication of nanoporous materials. Furthermore, due to its transparency, the nanoporous ITO electrode can operate as a platform for spectroelectrochemical studies that would allow us to observe the catalytic reaction phenomenon inside the nanopores.

(This work was originally published in *Electrochimica Acta*, 2017, 258, 90–97, DOI: 10.1016/j.electacta.2017.10.111)

Chapter 3.

Nanoporous ITO implemented Bipolar Electrode Sensor for enhanced Electrochemiluminescence

3.1 Introduction

Bipolar electrode (BPE) is a conducting electrode onto which faradaic reactions can be induced at its two ends without direct ohmic contact [75,76]. When electric potential (ΔE_{tot}) is applied to the solution in which the BPE is immersed, the BPE floats to an equilibrium potential, which is constant throughout the conductive BPE. The interfacial potential difference between the BPE and the solution varies along the BPE, and promotes electrochemical reactions at the two ends of the BPE (**Figure 3-1**). As charge must be conserved at the BPE, electron transfer rates must be the same for the cathode and anode pole.

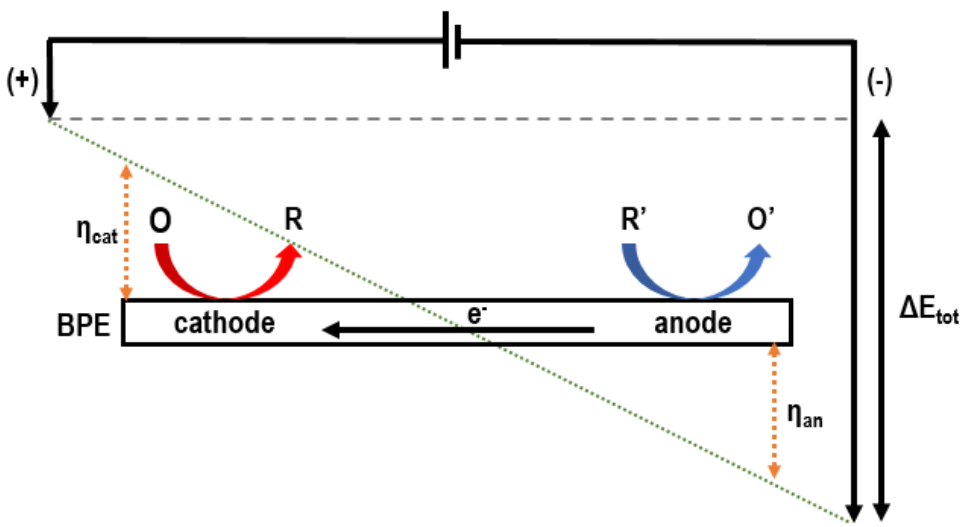

Figure 3-1. Scheme of bipolar electrodes. η_{cat} and η_{an} represent the cathodic and anodic overpotentials respectively.

BPEs are useful for constructing electronic manifolds, as the wireless character enables facile development of electrode arrays [77–79], multiplex systems [80], or application of other novel materials [81]. Consequently, BPE based systems have been expanded to chemical and biological sensors coupled with various reporting methods. While a number of reporting methods paired with BPE have been developed including colorimetry [82], fluorescence [83], and electrochemiluminiscence (ECL) [84–86], the ECL method is largely appreciated owing to its low background signal and high sensitivity [87]. After the first report from the Manz group to couple BPE with an ECL-based reporting system [88], phenomenal works from the Crooks group have successfully expanded the concept towards real sensing apparatuses [89]. Up to date, the advance in BPE-ECL sensors have enabled the analysis of various of key analytes, including biologically significant ions and molecules [90–92].

Indium tin oxides (ITOs) have been commonly used in sensors due to high conductivity, optical transmittance, wide electrochemical working windows, as well as their feasibility in patterning or surface modifying [93,94]. Due to their intrinsically low electrocatalytic ability, however, ITOs utilized in electrochemical sensors are usually modified by attaching catalytically active metals or enzymes [95–98], which may lead to additional cost and complicated manufacturing processes [99]. By introducing nanoporous structured ITOs, the low electrocatalytic activity of the ITO material could be complemented, as they possess larger surface areas and higher density of surface defects. Furthermore, additional catalytic abilities owing to their nanoporous morphology have been recently suggested [100]. While several studies have utilized nanoporous ITO electrodes as sensors without further surface modification [101–103], coupling to a BPE system has not been yet realized.

In this report, nanoporous ITO layers are implemented on the cathodic poles of BPEs by accumulation of ITO nanoparticles on patterned ITO substrates. The fabricated nanoporous ITO BPEs are utilized in detecting hydrogen peroxide (H_2O_2), using ECL as the readout signal. The nanoporous ITO layers resulted in reduction of the driving voltage and enhancement of ECL intensity, enabling detection with the naked eye under low functioning voltages. The effects of the nanoporous ITO structures towards H_2O_2 detection are further investigated by varying the nanoporous layer thickness, which could be done by tuning the number of spin coating process. We explored the reason for ECL enhancement in view of the morphology of ITO nanopores, as well as enlarged surface area.

3.2 Experimental

3.2.1 Chemicals and Materials

Acetic acid (≥ 99.7%, ACS reagent), potassium chloride (≥ 99.0%, ReagentPlus®), potassium phosphate dibasic, potassium phosphate monobasic, Tris(2,2′-bipyridyl) dichlororuthenium(II) hexahydrate ($Ru(bpy)_3Cl_2 \cdot 6H_2O$, 99.95% trace metals basis), tripropylamine (TPA, ≥99%) were purchased from Sigma Aldrich (St. Louis, Missouri, U.S.A.). Hydrogen peroxide (34.5 %) was purchased from Samchun Chemicals (South Korea). All reagents were used without further purification. All aqueous solutions in this experiment were prepared with ultrapure deionized water (resistivity ~18.2 MΩ) produced by NANO pure Diamond (Barnstead, New

Hampshire, U.S.A.).

H_2O_2 analyte solutions were prepared with 0.1 M phosphate buffered saline (PBS; pH 6.9) as the electrolyte, and the ECL solution consisted of 5 mM $Ru(bpy)_3^{2+}$ and 25 mM TPA in 0.1 M phosphate buffered saline (PBS; pH 6.9). ITO coated glass was purchased from Techinstro (Yadav Nagar, Nagpur Maharashtra, India). Silver wire (dia. 0.5 mm) and platinum wire (dia. 0.5 mm) were purchased from Sigma Aldrich (St. Louis, Missouri, U.S.A.).

For the chip fabrication and ITO etching process, Hexamethyldisilazane (HMDS) was obtained from J. T. Baker (Phillipsburg, New Jersey, U.S.A.), photoresist (PR; AZ 4620) and developer (AZ 400K) from Merck (Darmstadt, Germany), SU-8 from Microchem (Westborough, MA, U.S.A.), TIN etchant (TE-100) from Transene Company (Danvers, MA, U.S.A.). Poly(dimethylsiloxane) (PDMS) monomer and curing agent from Dow Corning (Midland, MI, U.S.A.), ITO nanoparticle powder (~30 nm diameter) from Lihochem (Taiwan).

3.2.2 Instruments

External voltage upon the BPE was applied by IviumStat electrochemical workstation (the Netherlands). Cyclic voltammetry and electrochemical impedance spectroscopy (EIS) in the three electrode system were performed by a CHI 604 potentiostat (CH Instruments, TX, U.S.A.) and Reference 600 (Gamry Instruments, PA, U.S.A.), respectively. For the three electrode systems, Ag/AgCl (3 M NaCl) and Pt wire was used as the reference and counter electrode respectively. The digital camera (Canon EOS 750D, ISO 6400) and microscope (Nikon TE2000U) were used for optical measurements of BPE.

The annealing process during nanoporous ITO fabrication was done with a tube furnace [Thermal CVD System, SciEnTech], and the morphology of the fabricated nanoporous ITO films was observed by focused ion beam (FIB) equipped with a field-emission scanning electron microscope (Helios 650, FEI, U.S.A.).

3.2.3 Fabrication of Nanoporous Indium Tin Oxide implemented BPEs

Microband patterned ITO electrodes with 22 mm length and 1 mm width were prepared beforehand by the ITO etching process. First, the ITO coated glass was subsequently cleaned with ethanol, acetone and deionized water, then dried by placing on 100 ℃ hot plate for 5 min. HMDS was spin coated on the ITO coated glass, and baked at 110 ℃ for 1.5 min, followed by PR spin coating and baking at 100 ℃ for 1.5 min. After being covered with a mask bearing the BPE pattern, the ITO glass was illuminated with UV light (365 nm) for 20 s. The PR pattern was developed with AZ 400K developer and baked at 120 ℃ for 15 min. Then, the exposed ITO was etched by immersing in the TE-100 etchant (pre heated at 65 ℃) for 15 min. Finally, remains of PR were eliminated with sonication in acetone.

ITO nanoparticles were deposited on the patterned ITO substrate by modifying a previously reported method [65]. First, the patterned ITO substrates were washed by sonication in acetone, isopropanol and water for 20 minutes each, followed by air plasma treatment in order to remove residual impurities. Meanwhile, the ITO nanoparticles were washed in acetone and ethanol several times, followed by dispersion in 5 M acetic acid/ethanol. To reduce the aggregated ITO nanoparticles, the dispersed ITO nanoparticles were mildly centrifuged several times, and the

resulting supernatant was used as the spin coating solution. Nanoporous ITO layers of varying thicknesses could be obtained by controlling the number of spin coating processes, where the spin coated substrates were placed on a hot plate at 100 ℃ for 10 min between each spin coating process. To ensure the formation of uniform nanoparticle layers, nanoporous ITO layers spin coated more than 2 times were studied in this work. The anodic pole (ECL reporting pole) of the BPE was covered by Kapton tape during the spin coating process, enabling selective deposition of ITO nanoparticles on the cathodic pole (H_2O_2 detecting pole). ITO nanoparticles deposited on regions other than the ITO pattern were carefully removed with Kapton tape and an ethanol swab. Afterwards, the films were annealed in two steps; first at 500℃ in atmospheric air for 1 h, and then at 300℃ in 5% H_2 / Argon gas for 1 h to raise the conductivity of the ITO films [67,68].

The mold for PDMS channels was prepared by the following steps. Silicon wafer was washed with piranha solution for 20 min and baked at 200 ℃ for 2 min. SU-8 was spin coated on the silicon wafer and baked at 65 ℃ for 2 min and at 95 ℃ for 7 min. The SU-8 layer was illuminated with UV light through a mask with a microchannel pattern for 20 s. Then, the SU-8 pattern was developed with SU-8 remover for 2 min. The patterned wafer was baked at 200℃ for 10 min, and 65℃ for 5 min.

For the fabrication of PDMS channels, the mold wafer was first attached to a petridish, and suitable amounts of PDMS monomer and curing agent (weight ratio 10:1) was poured on to the PDMS mold. Then it was placed in a 60 ℃ oven for 2 h. The resulting PDMS cover was cut to fit the shape of the ITO electrode substrate and small inlets of 1.5 mm diameter were drilled on both ends of the channel, where the feeder electrodes are to be placed.

Finally, the nanoporous ITO implemented BPE was completed by attaching the PDMS cover onto the nanoporous ITO implemented BPE, thus forming a microchannel.

3.2.4 Optical Analysis

The reporting and detecting channels of the nanoporous ITO BPE chip were filled with ECL solution and H_2O_2 solution, respectively. 0.1 M phosphate buffered saline (PBS) (pH 7.0) containing 5 mM $Ru(bpy)_3Cl_2 \cdot 6H_2O$ and 25 mM TPA constituted the ECL solution. H_2O_2 samples of different concentrations (2 μM to 5 mM) in 0.1 M PBS (pH 6.9) were independently prepared. For the detection of H_2O_2, constant potential (1.9 V) was applied to the two Ag/AgCl wires at the terminals with the aid of a potentiostat. Then, the ECL images were obtained in a dark room with a digital camera with an exposure time of 10 s. The ECL intensities were analyzed and quantified using the ImageJ software.

3.2.5 Electrochemical Methods

Conventional electrochemical experiments with nanoporous ITO electrodes was conducted by a 3- electrode system with Ag/AgCl (3 M NaCl) and Pt wire as the reference electrode and the counter electrode, respectively. The electrical contact of nanoporous ITO electrodes was made by aluminum conductive tape on the ITO substrate, and a portion of the electrode was exposed to the test solution by using an electroplating tape (3M™ Electroplating Tape 470). Electrochemical impedance

spectroscopy (EIS) measurements were carried out over a frequency range of 10 kHz to 0.05 Hz, with an AC input of 10 mV amplitude superimposed on the DC offset potential.

3.3 Results and Discussion

3.3.1 Design of the BPE microchip and the sensing system

The BPE microchip is composed of the following, as shown in **Figure 3-2 (a)**. The transparent PDMS cover with 90 μm deep microchannels form the closed BPE channel, while separating the detecting and reporting channels. The nanoporous ITO layer cathodic pole operates as the H_2O_2 detection cathode, whereas the bare ITO anodic pole is used as the ECL reporting electrode. Two AgCl/Ag wires used as driving electrodes are immersed in the inlets (diameter of 1.5 mm) drilled on both ends of the PDMS microchannel, ensuring regulated distance between the wires with the ITO electrodes.

Detection of H_2O_2, an important marker of metabolism, was conducted with the nanoporous ITO based BPE microchip, using electrochemiluminescence (ECL) as the readout signal (**Figure 3-2 (b)**). When a total potential (ΔE_{tot}) is applied by the driving electrode, uniform electric field is generated throughout the electrolyte. The electrode potential (ΔE_{elec}) is determined by the ratio of the length of the electrode and the channel. As the oxidation of $Ru(bpy)_3^{2+}$ is coupled with the reduction of H_2O_2, ECL emission depending on the concentration of H_2O_2 could be observed.

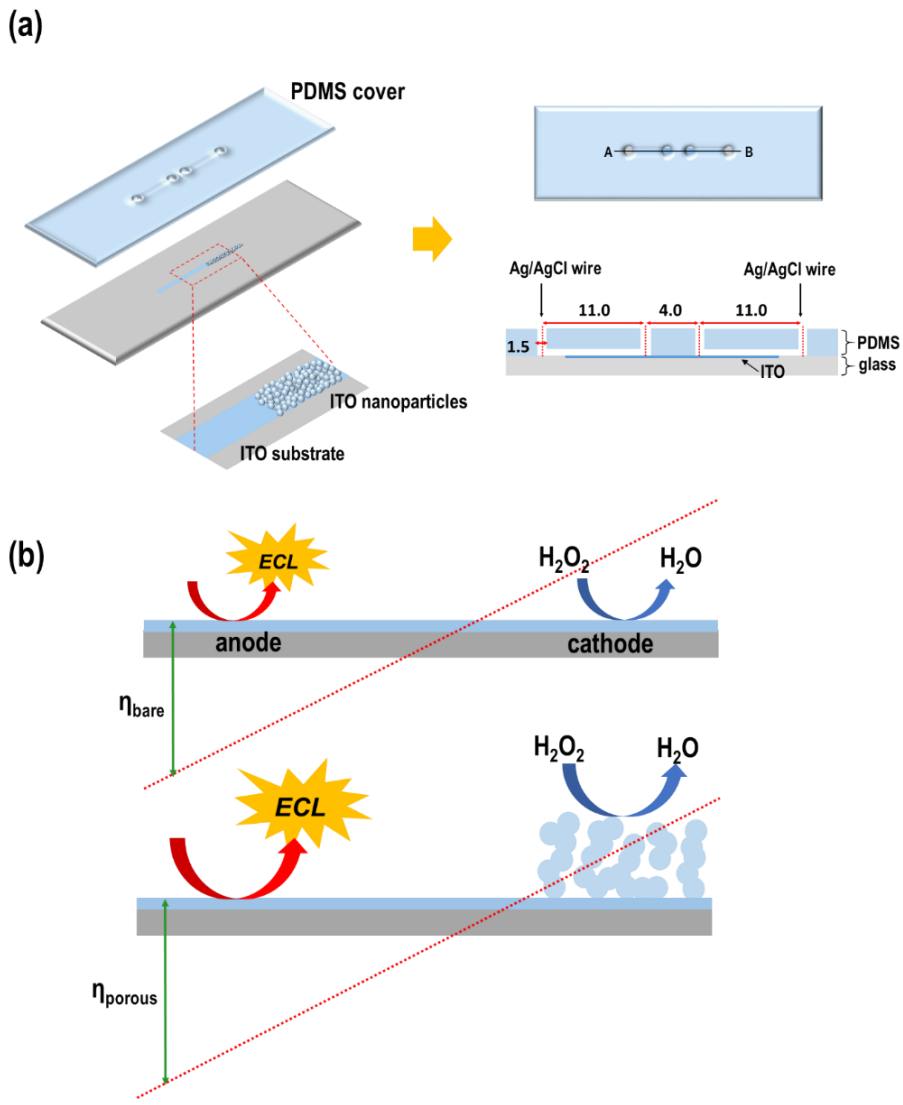

Figure 3-2. (a) Design of the nanoporous BPE microchip. The upper right-hand figure shows the top view of the BPE system, whereas the lower right-hand figure depicts the cross section of the BPE system along line AB. The units of measurements are in mm. (b) Schematic diagram of the H_2O_2 sensing system involving the BPE. (η: overpotential applied on the anodic poles of BPE)

3.3.2 Characterization of nanoporous Indium Tin Oxide layer

In order to characterize the nanoporous ITO layers formed on the BPE, ITO nanoparticles were also deposited upon non-patterned, planar ITO substrates under the same spin coating conditions. These samples were used to observe the morphology of the nanoporous ITOs as well as for electrochemical characterization. The morphologies of the resulting nanoporous ITO electrodes were first examined by FESEM (field emission scanning electron microscope) (**Figure 3-3**). The cross section FESEM images obtained by FIB (focused ion beam) methods show the porous structure of the electrodes, formed by the accumulation of ITO nanoparticles. The pores sizes range from several tens to a hundred nanometers, and the porous layer thickness increase regularly with the number of repeated spin coating process (roughly 85 nm per spin coating). Throughout the paper, we will denote the nanoporous ITO electrodes 'ITO xn', where the 'n' represents the number of spin coating processes.

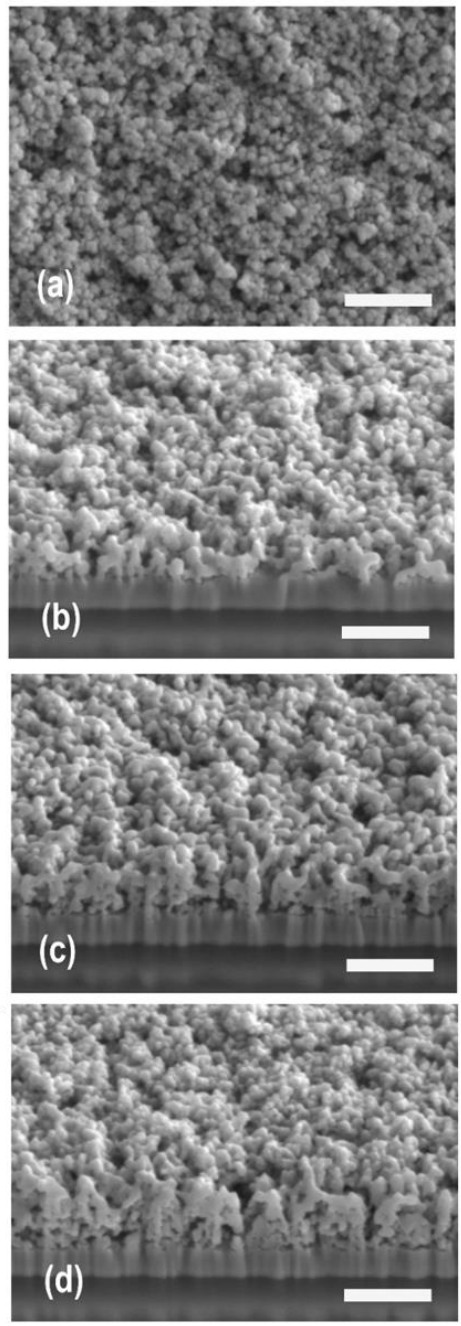

Figure 3-3 (a) Top view Field-Emission Scanning Electron Microscope (FESEM) of nanoporous ITO electrode spin coated 2 times. Cross section FESEM images of electrodes spin coated (b) 2 times, (c) 3 times, and (d) 4 times. The scale bar represents 500 nm.

The electrochemical active surface area (ECSA) of the fabricated nanoporous ITO electrodes could be estimated from the charging currents measured by cyclic voltammetry. First, the cyclic voltammograms were obtained in 0.1 M phosphate buffered saline solution, with varying scan rates of 10, 20, 50, 100 mV/s. As expected, the charging current steadily escalated with the increasing nanoporous ITO layer, ensuring the conductivity of the nanoporous electrodes as well as the good accessibility of ions into the nanopores **(Figure 3-4 (a)**). The relative ECSA values could be quantified by plotting the charging current against the scan rate, and obtaining the slope values (**Figure 3-4 (b)**). The relative ECSA values were calculated by dividing the slope values obtained from of ITO x2, ITO x3 and ITO x4 electrodes with those of the bare ITO [104]. The slope and calculated relative ECSA values are summarized in **Table 3-1**.

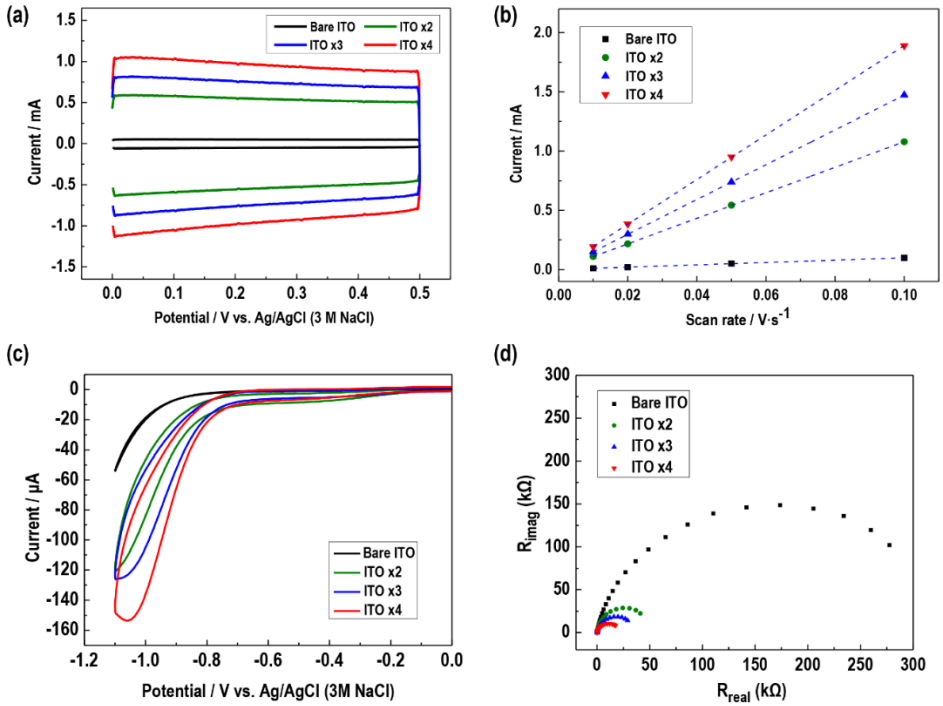

Figure 3-4 (a) The charging current of nanoporous ITO electrodes measured by cyclic voltammetry in 0.1 M phosphate buffered saline solution, scan rate 50 mV/s. (b) The charging current obtained by the average of anodic and cathodic charging currents at 0.250 V (vs. Ag/AgCl (3 M NaCl)) are plotted against various scan rates (10, 20, 50, 100 mV/s). (c) Cyclic Voltammogram of bare ITO, ITO x2, ITO x3 and ITO x4 electrodes in 5 mM H_2O_2, scan rate 50 mV/s. (d) Electrochemical impedance spectroscopy (EIS) data of bare ITO, ITO x2, ITO x3 and ITO x4 electrodes in 5 mM H_2O_2, where the DC potential is set to -0.75 V.

Electrode	Slope	Relative ECSA
Bare ITO	9.91×10^{-7}	1.00
ITO x2	1.08×10^{-5}	10.9
ITO x3	1.47×10^{-5}	14.8
ITO x4	1.88×10^{-5}	19.0

Table 3-1. The slope of the plot shown in **Figure 3-3 (b)** and relative ECSA values of Bare ITO electrode, ITO x2, ITO x3 and ITO x4 electrodes.

The electrocatalytic properties of the nanoporous ITO electrodes towards H_2O_2 reduction were observed by cyclic voltammetry and electrochemical impedance spectroscopy (EIS). **Figure 3-4 (c)** show the cyclic voltammetry of the bare ITO and the nanoporous ITO x2, x3 and x4 electrodes measured in 5 mM H_2O_2. The cathodic current increased notably for the nanoporous ITO electrodes in comparison to the bare ITO electrode, and the onset potential shifted towards positive values. The EIS measurement data shown in **Figure 3-4 (d)** display similar trends, as indicated by considerable resistance decrease with a thicker porous ITO layers.

3.3.3 Optical analysis of H_2O_2 detection

The development of reliable, sensitive and low cost methods for H_2O_2 detection is of practical importance, as H_2O_2 is known to be involved in numerous biological events such as cellular functions and signal transduction processes [105]. H_2O_2 detection with the modified BPEs was performed to observe effects of the nanoporous ITO electrodes. Three kinds of BPE microchip with different porous layers thicknesses (ITO x2, ITO x3, and ITO x4), and the unmodified, bare ITO BPE were utilized for the H_2O_2 detection. The ECL images obtained for 5 mM H_2O_2 are shown in **Figure 3-5 (a)**, where stronger ECL signals with the consecutive deposition of nanoporous ITO layers can be clearly observed. This indicates that BPEs implemented with nanoporous ITO layers can operate under weaker driving voltages than that required for the bare ITO BPEs. This feature was exemplified in **Figure 3-5 (b)**, where ECL signal intensities of the BPEs towards 5 mM H_2O_2 are plotted depending on the driving voltage. As seen in the inset of **Figure 3-5 (b)**, a clear decrease in the onset potential could be observed for BPEs with thicker nanoporous ITO layers. However, the ECL intensity at the blank solution (with no H_2O_2 analyte) also increased considerably when the potential was raised above 2.0 V, presumably due to increase in side reactions such as hydrogen evolution reactions, or oxygen reduction (**Figure 3-6**). Thus, for effective and accurate assessment of the H_2O_2 analyte, we chose 1.9 V as the driving voltage in our BPE system.

.

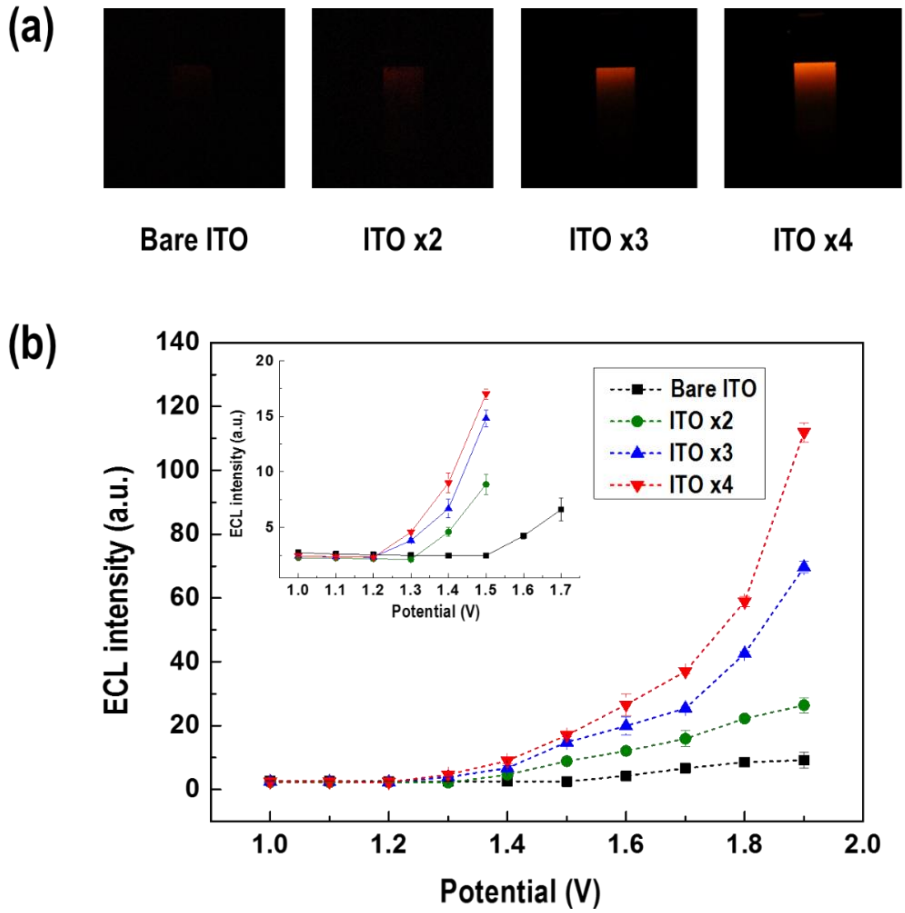

Figure 3-5 H_2O_2 sensing system with four BPEs with different depths of ITO nanoporous layers. (a) ECL images obtained from a 5 mM H_2O_2 solution under constant voltage of 1.9 V (b) ECL intensities of BPEs from 5 mM H_2O_2 depending on the applied voltage, where the inset shows the enlarged view of ECL intensities at mild potentials

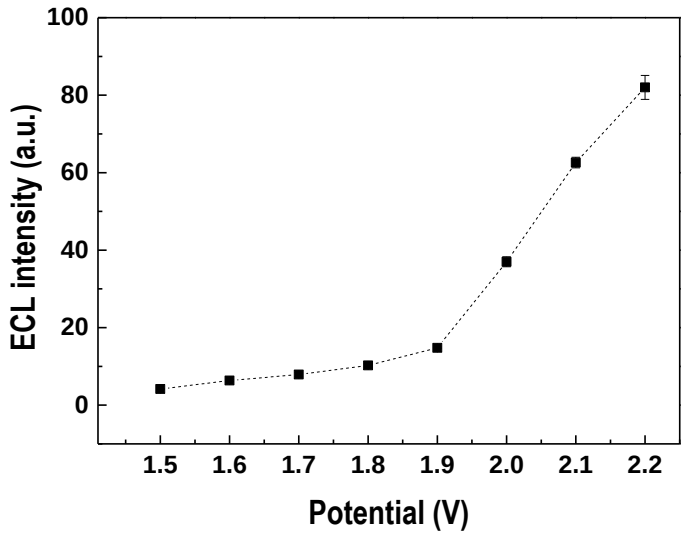

Figure 3-6 ECL intensities depending on the applied voltage, measured from x4 ITO implemented BPE with bare 0.1 M phosphate buffered saline solution.

ECL intensities of the BPEs were observed with concentration of H_2O_2 ranging from 2 μM to 5 mM (**Figure 3-7**). A good linear response was shown between the ECL intensity and the logarithm of H_2O_2 concentration. The overall signal intensities and the slope of the calibration curve increased with the thickening nanoporous ITO layer, indicating enhanced activity of nanoporous ITO electrodes towards H_2O_2 reduction. The linear ranges and the limit of detection (LOD) values acquired from the calibration curve of **Figure 3-7** are summarized in **Table 3-2**. The LOD was calculated as the H_2O_2 concentration with the signal three standard deviations above the blank solution. The LOD values continually decrease with the increasing nanoporous ITO layer, with 21.86 μM as the lowest LOD value for the ITO x4 electrode. The extent in change of LODs upon the nanoporous layer demonstrates the effect of nanoporous structure towards the signal intensity and detecting sensitivity of the BPEs.

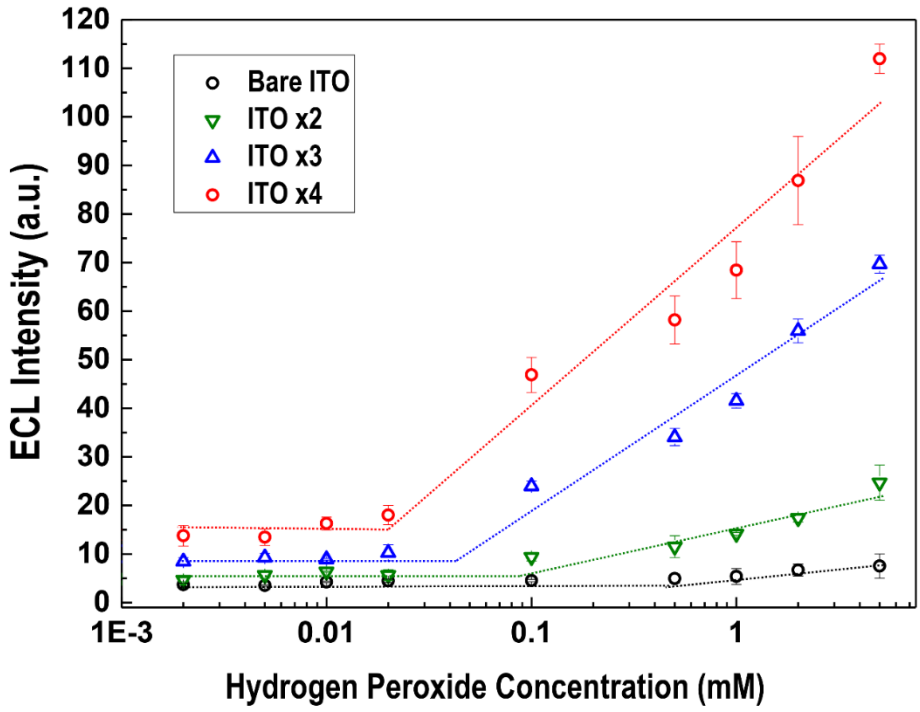

Figure 3-7 ECL intensities depending on the analyte (H_2O_2) concentration. The dotted lines are added to guide the linear range.

Electrode	Linear range (mM)	LOD (µM)
Bare ITO	0.5 – 5	271.97
ITO x2	0.1 – 5	70.42
ITO x3	0.1 – 5	43.98
ITO x4	0.02 – 5	21.86

Table 3-2 The linear range and LOD of nanoporous ITO implemented BPEs

One of the reasons for the ECL enhancement in nanoporous ITO based BPEs would be the enlarged surface area of the cathode, where the nanoporous layer is selectively deposited. Previous studies have reported enhaced ECL intensities upon tuning the relative areas of the anode and cathode [89,106,107]. As depicted in **Figure 3-2 (b)**, the relatively large area of the cathode (nanoporous ITO) compared to the anode (bare ITO) would shift the electric field of the BPE. This leads to increased anodic overpotential, hence accounting for the enhanced ECL with thicker nanoporous ITO layers, under identical operating voltages.

3.3.4 Nanoconfinement effects of nanoporous structures towards H_2O_2 detection

We further explored the principles behind the ECL enhancement of nanoporous ITO BPEs with regard to their structural characteristics and their electrocatalytic effects towards H_2O_2 reduction. Nanoporous structured electrodes can confine reactant molecules inside its nanopores, leading to augmented interaction between the reactant with the electrode surface, resulting in increased electrochemical rates. This catalytic mechanism based on the nanoporous morphologies have been suggested by previous reports, denoted as 'nanoconfinement effect' [37,100].

Comparing the kinetics of H_2O_2 reduction with nanoporous ITO BPEs of differing layer thicknesses would enable us to observe the nanoconfinement effects stemming from the nanoporous morphology. As the extent of H_2O_2 reduction taking place at the nanoporous ITO layer (the cathodic pole) is reflected by the ECL signal intensity at the opposite anodic pole, the catalytic effects of the nanoporous ITO layers could be determined without directly measuring the faradaic current of the cathodic electrode. In order to assess and compare the ECL signal intensities while excluding effects due to the enlarged surface areas of the nanoporous ITOs, the ECL intensities of the nanoporous ITO based BPEs (formerly shown in **Figure 3-7**) were normalized by their relative ECSA values (listed in **Table 3-1**) respectively. The normalized ECL intensities of the ITO x2, x3, and x4 implemented BPEs for the various H_2O_2 concentrations are shown in **Figure 3-8 (a)**. The ITO x3 and ITO x4 BPEs exhibit higher ECL intensities than those of the bare ITO BPE, and the ECL signal enhances with the increasing thickness of nanoporous ITO layers.

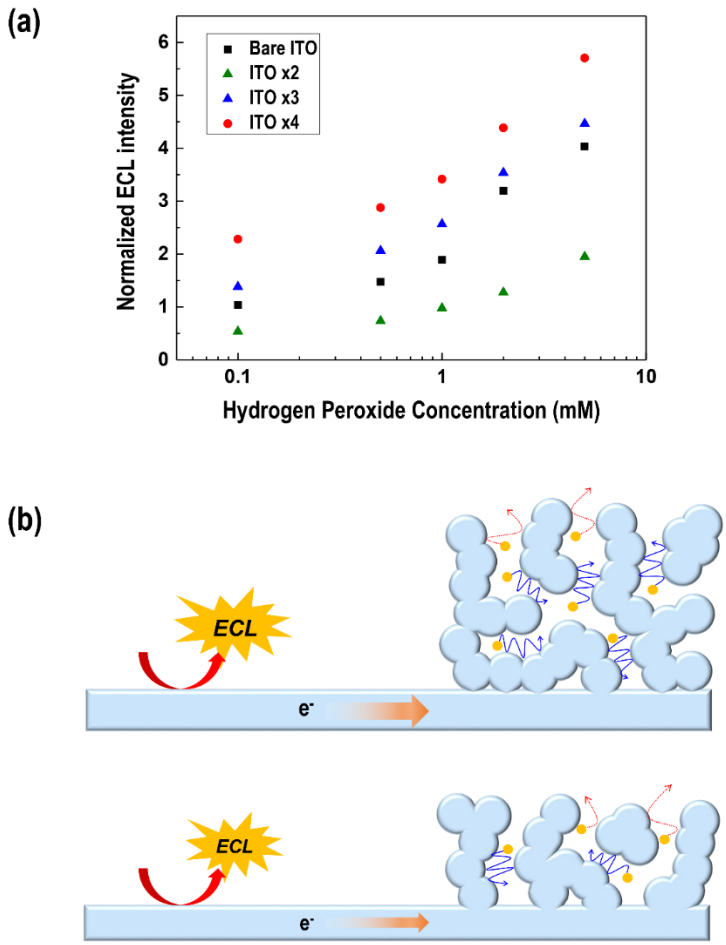

Figure 3-8 (a) ECL intensities of bareITO, ITO x2, x3, and x4 implemented BPEs, normalized by the relative ECSA values through the following equation; Normalized ECL intensity = {(Measured ECL intensity) – (Background ECL intensity)} / (ECSA value). The 'background ECL intensity', which is the light intensity under which no voltage is applied to the BPE, is subtracted to eliminate the background noise. (b) Possible scheme of reactants in the nanoconfined space of nanoporous ITO layers. The orange circles represent the reactant molecules, and the arrows represent simplified trajectories of the reactants. The blue, solid arrows demonstrate increased interaction between the reactant molecules and the electrode due to nanoconfinement effects. The red dashed arrows depict reactants at the shallow regions of the nanoporous structure, which are less likely to be confined in the nanopores.

Due to normalization of ECL intensity with respect to the surface area, the remaining difference in catalytic factor between the varying nanoporous electrodes is the extent of the 'nanoconfined space'. Thus, the enhanced normalized ECL signal with increasing nanoporous ITO layers suggests that the confined space of nanopores contribute to the H_2O_2 reduction activity. This scheme is depicted in **Figure 3-8 (b)**. The thicker nanoporous layers with larger proportion of deep nanopores (i.e. extended nanoconfined space) would show intensified nanoconfinement effects, resulting in facilitated faradaic reactions.

Hence, we have investigated the nanoconfinement effects towards H_2O_2 reduction exhibited by enhanced ECL signals of nanoporous ITO imbedded BPEs. This is the first attempt in verifying nanoconfinement effects in such systems, where the faradaic currents of nanoporous electrodes are not directly measured.

3.4 Conclusion

We have developed a novel, nanoporous ITO BPE based sensing system in which the cathode is modified with a nanoporous ITO layer, resulting in enhanced LODs and sensitivities toward H_2O_2 detection. Additional improvements in detection could be achieved by increasing the nanoporous ITO layer thickness. No other surface modifications on the ITOs, such as metal nanoparticles or enzyme attachment were needed, bypassing any concerns of cost issues or performance failures due to surface fouling. The increased efficiency in sensing abilities enabled the BPEs to detect H_2O_2 with a relatively mild potential of 1.9 V. In further investigation of the enhanced sensing abilities of the nanoporous ITO BPE, we indirectly observed the existence of nanoconfinement effects from nanoporous electrodes with the aid of the BPE-ECL system.

As ECL is widely utilized as a reporting method through the BPE sensors electrochemical analysis, the development of highly sensitive electrodes based on its nanostructures would assist in the construction of sensing devices that enable direct interpretation with the naked eye. Accompanied by advantages with regard to moderate operating voltage, this system proves as a promising candidate to be further extended to portable or in situ sensing devices.

(This work was originally published in *Electrochimica Acta*, 2019, 314, 89–95, DOI: 10.1016/j.electacta.2019.05.052)

Chapter 4.

Conclusions and Perspective

With the advent of environmental issues and increasing demands for medical monitoring devices, highly efficient, yet cost-effective and stable electrocatalysts are essential nowadays. A representative catalyst design strategy involves optimizing electronic structure of noble metal materials based on activity descriptors such as surface adsorption energies. As a result, the effects of various surface modification methods upon electrocatalyst performance have been extensively investigated, including metal alloys, core-shell structures *etc*. Accordingly, fabrication of nanostructured electrocatalysts have also attracted attention due to their enlarged surface-to-volume, surface defects and altered crystalline facets, that lead to enhanced catalytic activities.

However, considering that electron transfer processes occur between two different phases (mostly between the liquid phase, where the reactants are positioned, and the solid electrode phase), there is comparatively little attention towards the environment of the liquid phase and its influence towards the electron transfer process. Specifically, when the nanoscale morphology forms a confined space, the liquid phase inside the pores are placed in a unique environment, where a small volume of space is surrounded by the inner electrode walls that are separated by merely several nanometers. In this case, not only are the reactant molecules confined within close distance with the electrode surface, but the proportion of the solution volume near the electrode surface increases exceedingly. It has been previously suggested that the confinement of reactants to close proximity with the electrode surface leads to altered molecular properties and reaction parameters, denoted as the nanoconfinement effect.

Several studies have been made regarding nanoconfinement effects in electrochemistry, most of which employ nanoporous electrodes fabricated with noble metals such as platinum or gold. By using such materials, intricate and well-controlled pores in the nanoscale could be feasibly fabricated and investigated.

However, using nanostructured Pt or Au have some disadvantages in studying the confinement effects. For instance, the catalytic activity of nanoporous Pt or Au electrodes would appear as a mixture of catalytic factors including nanoporous structure as well as additional surface characteristics (including surface defects or altered facets) of the noble catalysts. Also, the highly adsorptive behavior of noble metals would impact the catalytic pathway.

In the first part of this thesis, nanoporous electrodes fabricated with materials of low activity (indium tin oxide) were employed in order to isolate catalytic effects stemming from the nanoporous structure. Also, to exclude catalytic effects coming from rough surfaces, ITO nanoporous electrodes of varying nanoporous thicknesses were compared. Using electrochemical impedance spectroscopy (EIS) as a tool, kinetic constants of single electron transfer of $Fe^{2+/3+}$ exhibited enhancement upon increasing nanoporous layer thickness, reflecting the role of confined space upon electron transfer kinetics. In the second part of the thesis, nanoporous ITO layers were utilized in sensing hydrogen peroxide via bipolar electrode system. Likewise, the sensitivity of the BPE based sensor, indicated by the electrochemiluminescence (ECL) intensity, was found to be improved with the thickening nanoporous ITO layer. This result demonstrated the possibility of boosting sensor performance by nanostructure modification, even without the aid of implementing enzymes or noble materials.

Elucidating catalytic phenomena inside nanopores of electrocatalysts is challenging in many aspects. The confined geometry is expected to induce various phenomena other than molecular dynamics, for instance, altered solvent characteristics, or modified electric fields coming from the extreme curvature of electrodes. Directly observing catalytic environment inside the pores cause difficulty and limitations in selecting nanoporous materials, reactant molecules and analysis tools. A combination of electrochemical methods, along with spectroscopical tools

with appropriate probe molecules, and suitable models would aid in elucidating environmental factors and their impact towards electrochemical kinetics.

References

[1] Trasatti, S. Electrocatalysis in the Anodic Evolution of Oxygen and Chlorine. *Electrochimica Acta*, **1984**, *29*, 1503–1512.

[2] Stamenkovic, V.R.; Mun, B.S.; Arenz, M.; Mayrhofer, K.J.J.; Lucas, C.A.; Wang, G.; Ross, P.N.; Markovic, N.M. Trends in Electrocatalysis on Extended and Nanoscale Pt-Bimetallic Alloy Surfaces. *Nat. Mater.*, **2007**, *6*, 241–247.

[3] Ruban, A.; Hammer, B.; Stoltze, P.; Skriver, H.L.; Nørskov, J.K. Surface Electronic Structure and Reactivity of Transition and Noble Metals1Communication Presented at the First Francqui Colloquium, Brussels, 19–20 February 1996.1. *J. Mol. Catal. Chem.*, **1997**, *115*, 421–429.

[4] Stephens, I.E.L.; Bondarenko, A.S.; Grønbjerg, U.; Rossmeisl, J.; Chorkendorff, I. Understanding the Electrocatalysis of Oxygen Reduction on Platinum and Its Alloys. *Energy Environ. Sci.*, **2012**, *5*, 6744–6762.

[5] Kuttiyiel, K.A.; Choi, Y.; Hwang, S.-M.; Park, G.-G.; Yang, T.-H.; Su, D.; Sasaki, K.; Liu, P.; Adzic, R.R. Enhancement of the Oxygen Reduction on Nitride Stabilized Pt-M (M=Fe, Co, and Ni) Core–Shell Nanoparticle Electrocatalysts. *Nano Energy*, **2015**, *13*, 442–449.

[6] Wang, C.; Daimon, H.; Onodera, T.; Koda, T.; Sun, S. A General Approach to the Size- and Shape-Controlled Synthesis of Platinum Nanoparticles and Their Catalytic Reduction of Oxygen. *Angew. Chem. Int. Ed.*, **2008**, *47*, 3588–3591.

[7] Chen, C.; Kang, Y.; Huo, Z.; Zhu, Z.; Huang, W.; Xin, H.L.; Snyder, J.D.; Li, D.; Herron, J.A.; Mavrikakis, M.; Chi, M.; More, K.L.; Li, Y.; Markovic, N.M.; Somorjai, G.A.; Yang, P.; Stamenkovic, V.R. Highly Crystalline Multimetallic Nanoframes with Three-Dimensional Electrocatalytic Surfaces. *Science*, **2014**, *343*, 1339–1343.

[8] Zhang, L.; Roling, L.T.; Wang, X.; Vara, M.; Chi, M.; Liu, J.; Choi, S.-I.; Park, J.; Herron, J.A.; Xie, Z.; Mavrikakis, M.; Xia, Y. Platinum-Based Nanocages with Subnanometer-Thick Walls and Well-Defined, Controllable Facets.

Science, **2015**, *349*, 412–416.

[9] Evans, S.A.G.; Elliott, J.M.; Andrews, L.M.; Bartlett, P.N.; Doyle, P.J.; Denuault, G. Detection of Hydrogen Peroxide at Mesoporous Platinum Microelectrodes. *Anal. Chem.*, **2002**, *74*, 1322–1326.

[10] Asefa, T. Metal-Free and Noble Metal-Free Heteroatom-Doped Nanostructured Carbons as Prospective Sustainable Electrocatalysts. *Acc. Chem. Res.*, **2016**, *49*, 1873–1883.

[11] Li, D.; Wang, C.; Strmcnik, D.S.; Tripkovic, D.V.; Sun, X.; Kang, Y.; Chi, M.; Snyder, J.D.; Vliet, D. van der; Tsai, Y.; Stamenkovic, V.R.; Sun, S.; Markovic, N.M. Functional Links between Pt Single Crystal Morphology and Nanoparticles with Different Size and Shape: The Oxygen Reduction Reaction Case. *Energy Environ. Sci.*, **2014**, *7*, 4061–4069.

[12] Fujita, T.; Guan, P.; McKenna, K.; Lang, X.; Hirata, A.; Zhang, L.; Tokunaga, T.; Arai, S.; Yamamoto, Y.; Tanaka, N.; Ishikawa, Y.; Asao, N.; Yamamoto, Y.; Erlebacher, J.; Chen, M. Atomic Origins of the High Catalytic Activity of Nanoporous Gold. *Nat. Mater.*, **2012**, *11*, 775–780.

[13] Dubau, L.; Lopez-Haro, M.; Castanheira, L.; Durst, J.; Chatenet, M.; Bayle-Guillemaud, P.; Guétaz, L.; Caqué, N.; Rossinot, E.; Maillard, F. Probing the Structure, the Composition and the ORR Activity of Pt3Co/C Nanocrystallites during a 3422h PEMFC Ageing Test. *Appl. Catal. B Environ.*, **2013**, *142–143*, 801–808.

[14] Camara, G.A.; Ticianelli, E.A.; Mukerjee, S.; Lee, S.J.; McBreen, J. The CO Poisoning Mechanism of the Hydrogen Oxidation Reaction in Proton Exchange Membrane Fuel Cells. *J. Electrochem. Soc.*, **2002**, *149*, A748.

[15] Ramli, Z.A.C.; Kamarudin, S.K. Platinum-Based Catalysts on Various Carbon Supports and Conducting Polymers for Direct Methanol Fuel Cell Applications: A Review. *Nanoscale Res. Lett.*, **2018**, *13*.

[16] Banerjee, S.; Zare, R.N. Syntheses of Isoquinoline and Substituted Quinolines in Charged Microdroplets. *Angew. Chem.*, **2015**, *127*, 15008–15012.

[17] Lee, J.K.; Kim, S.; Nam, H.G.; Zare, R.N. Microdroplet Fusion Mass Spectrometry for Fast Reaction Kinetics. *Proc. Natl. Acad. Sci. U. S. A.*, **2015**, *112*, 3898–3903.

[18] Banerjee, S.; Gnanamani, E.; Yan, X.; N. Zare, R. Can All Bulk-Phase Reactions Be Accelerated in Microdroplets? *Analyst*, **2017**, *142*, 1399–1402.

[19] Mondal, S.; Acharya, S.; Biswas, R.; Bagchi, B.; Zare, R.N. Enhancement of Reaction Rate in Small-Sized Droplets: A Combined Analytical and Simulation Study. *J. Chem. Phys.*, **2018**, *148*, 244704.

[20] Wheeldon, I.; Minteer, S.D.; Banta, S.; Barton, S.C.; Atanassov, P.; Sigman, M. Substrate Channelling as an Approach to Cascade Reactions. *Nat. Chem.*, **2016**, *8*, 299–309.

[21] Dunn, M.F.; Aguilar, V.; Brzovic, P.; Drewe, W.F.; Houben, K.F.; Leja, C.A.; Roy, M. The Tryptophan Synthase Bienzyme Complex Transfers Indole between the .Alpha.- and .Beta.-Sites via a 25-30 .ANG. Long Tunnel. *Biochemistry*, **1990**, *29*, 8598–8607.

[22] Benedetti, T.M.; Andronescu, C.; Cheong, S.; Wilde, P.; Wordsworth, J.; Kientz, M.; Tilley, R.D.; Schuhmann, W.; Gooding, J.J. Electrocatalytic Nanoparticles That Mimic the Three-Dimensional Geometric Architecture of Enzymes: Nanozymes. *J. Am. Chem. Soc.*, **2018**, *140*, 13449–13455.

[23] Li, P.; Cao, C.-Y.; Chen, Z.; Liu, H.; Yu, Y.; Song, W.-G. Core–Shell Structured Mesoporous Silica as Acid–Base Bifunctional Catalyst with Designated Diffusion Path for Cascade Reaction Sequences. *Chem. Commun.*, **2012**, *48*, 10541–10543.

[24] Yen, C.W.; Mahmoud, M.A.; El-Sayed, M.A. Photocatalysis in Gold Nanocage Nanoreactors. *J. Phys. Chem. A*, **2009**, *113*, 4340–4345.

[25] Mahmoud, M.A.; Saira, F.; El-Sayed, M.A. Experimental Evidence For The Nanocage Effect In Catalysis With Hollow Nanoparticles. *Nano Lett.*, **2010**, *10*, 3764–3769.

[26] Mahmoud, M.A.; Narayanan, R.; El-Sayed, M.A. Enhancing Colloidal

Metallic Nanocatalysis: Sharp Edges and Corners for Solid Nanoparticles and Cage Effect for Hollow Ones. *Acc. Chem. Res.*, **2013**, *46*, 1795–1805.

[27] White, R.J.; White, H.S. A Random Walk through Electron-Transfer Kinetics. *Anal. Chem.*, **2005**, *77*, 214 A-220 A.

[28] Huang, K.-C.; White, R.J. Random Walk on a Leash: A Simple Single-Molecule Diffusion Model for Surface-Tethered Redox Molecules with Flexible Linkers. *J. Am. Chem. Soc.*, **2013**, *135*, 12808–12817.

[29] Malek, K.; Coppens, M.-O. Effects of Surface Roughness on Self- and Transport Diffusion in Porous Media in the Knudsen Regime. *Phys. Rev. Lett.*, **2001**, *87*.

[30] Malek, K.; Coppens, M.-O. Knudsen Self- and Fickian Diffusion in Rough Nanoporous Media. *J. Chem. Phys.*, **2003**, *119*, 2801–2811.

[31] Debe, M.K. Effect of Electrode Surface Area Distribution on High Current Density Performance of PEM Fuel Cells. *J. Electrochem. Soc.*, **2011**, *159*, B53–B66.

[32] Debe, M.K. Tutorial on the Fundamental Characteristics and Practical Properties of Nanostructured Thin Film (NSTF) Catalysts. *J. Electrochem. Soc.*, **2013**, *160*, F522–F534.

[33] Marcus, R.A. On the Theory of Electron-Transfer Reactions. VI. Unified Treatment for Homogeneous and Electrode Reactions. *J. Chem. Phys.*, **1965**, *43*, 679–701.

[34] Hupp, J.T.; Weaver, M.J. The Frequency Factor for Outer-Sphere Electrochemical Reactions. *J. Electroanal. Chem. Interfacial Electrochem.*, **1983**, *152*, 1–14.

[35] Katsounaros, I.; B. Schneider, W.; C. Meier, J.; Benedikt, U.; Ulrich Biedermann, P.; A. Auer, A.; J. Mayrhofer, K.J. Hydrogen Peroxide Electrochemistry on Platinum: Towards Understanding the Oxygen Reduction Reaction Mechanism. *Phys. Chem. Chem. Phys.*, **2012**, *14*, 7384–7391.

[36] Nie, Y.; Li, L.; Wei, Z. Recent Advancements in Pt and Pt-Free Catalysts for

Oxygen Reduction Reaction. *Chem. Soc. Rev.*, **2015**, *44*, 2168–2201.

[37] Han, J.-H.; Lee, E.; Park, S.; Chang, R.; Chung, T.D. Effect of Nanoporous Structure on Enhanced Electrochemical Reaction. *J. Phys. Chem. C*, **2010**, *114*, 9546–9553.

[38] Bae, J.H.; Han, J.-H.; Chung, T.D. Electrochemistry at Nanoporous Interfaces: New Opportunity for Electrocatalysis. *Phys. Chem. Chem. Phys.*, **2011**, *14*, 448–463.

[39] Bae, J.H.; Han, J.-H.; Han, D.; Chung, T.D. Effects of Adsorption and Confinement on Nanoporous Electrochemistry. *Faraday Discuss.*, **2013**, *164*, 361–376.

[40] Senapati, S.; Chandra, A. Dielectric Constant of Water Confined in a Nanocavity. *J. Phys. Chem. B*, **2001**, *105*, 5106–5109.

[41] Baumann, R.; Ferrante, C.; Kneuper, E.; Deeg, F.-W.; Bräuchle, C. Influence of Confinement on the Solvation and Rotational Dynamics of Coumarin 153 in Ethanol. *J. Phys. Chem. A*, **2003**, *107*, 2422–2430.

[42] Thompson, W.H. Solvation Dynamics and Proton Transfer in Nanoconfined Liquids. *Annu. Rev. Phys. Chem.*, **2011**, *62*, 599–619.

[43] Itoh, H.; Sakuma, H. Dielectric Constant of Water as a Function of Separation in a Slab Geometry: A Molecular Dynamics Study. *J. Chem. Phys.*, **2015**, *142*, 184703.

[44] Fumagalli, L.; Esfandiar, A.; Fabregas, R.; Hu, S.; Ares, P.; Janardanan, A.; Yang, Q.; Radha, B.; Taniguchi, T.; Watanabe, K.; Gomila, G.; Novoselov, K.S.; Geim, A.K. Anomalously Low Dielectric Constant of Confined Water. *Science*, **2018**, *360*, 1339–1342.

[45] Baumann, R.; Ferrante, C.; Deeg, F.W.; Bräuchle, C. Solvation Dynamics of Nile Blue in Ethanol Confined in Porous Sol–Gel Glasses. *J. Chem. Phys.*, **2001**, *114*, 5781–5791.

[46] Sun, M.; Dong, J.; Lv, Y.; Zhao, S.; Meng, C.; Song, Y.; Wang, G.; Li, J.; Fu, Q.; Tian, Z.; Bao, X. Pt@h-BN Core–Shell Fuel Cell Electrocatalysts with

Electrocatalysis Confined under Outer Shells. *Nano Res.*, **2018**, *11*, 3490–3498.

[47] Martínez de la Hoz, J.M.; Balbuena, P.B. Geometric and Electronic Confinement Effects on Catalysis. *J. Phys. Chem. C*, **2011**, *115*, 21324–21333.

[48] Birkin, P.R.; Elliott, J.M.; Watson, Y.E. Electrochemical Reduction of Oxygen on Mesoporous Platinum Microelectrodes. *Chem. Commun.*, **2000**, 1693–1694.

[49] Park, S.; Chung, T.D.; Kim, H.C. Nonenzymatic Glucose Detection Using Mesoporous Platinum. *Anal. Chem.*, **2003**, *75*, 3046–3049.

[50] Snyder, J.; McCue, I.; Livi, K.; Erlebacher, J. Structure/Processing/Properties Relationships in Nanoporous Nanoparticles As Applied to Catalysis of the Cathodic Oxygen Reduction Reaction. *J. Am. Chem. Soc.*, **2012**, *134*, 8633–8645.

[51] Han, J.-H.; Bae, J.H.; Han, D.; Chung, T.D. Confined Molecular Dynamics for Suppressing Kinetic Loss in Sugar Fuel Cell. *Electrochimica Acta*, **2016**, *187*, 457–464.

[52] Nazemi, M.; Panikkanvalappil, S.R.; El-Sayed, M.A. Enhancing the Rate of Electrochemical Nitrogen Reduction Reaction for Ammonia Synthesis under Ambient Conditions Using Hollow Gold Nanocages. *Nano Energy*, **2018**, *49*, 316–323.

[53] Bae, J.H.; Kim, Y.-R.; Kim, R.S.; Chung, T.D. Enhanced Electrochemical Reactions of 1,4-Benzoquinone at Nanoporous Electrodes. *Phys. Chem. Chem. Phys.*, **2013**, *15*, 10645–10653.

[54] Joo, S.H.; Choi, S.J.; Oh, I.; Kwak, J.; Liu, Z.; Terasaki, O.; Ryoo, R. Ordered Nanoporous Arrays of Carbon Supporting High Dispersions of Platinum Nanoparticles. *Nature*, **2001**, *412*, 169–172.

[55] Seo, B.; Kim, J. Electrooxidation of Glucose at Nanoporous Gold Surfaces: Structure Dependent Electrocatalysis and Its Application to Amperometric Detection. *Electroanalysis*, **2010**, *22*, 939–945.

[56] Cho, Y.-B.; Kim, J.E.; Lee, C.; Lee, Y. Electroactivity of Nanoporous Platinum Depending on the Porosity and Potential for Various Electrode Reactions. *J.*

Electroanal. Chem., **2016**, *768*, 121–128.

[57] Menshykau, D.; Compton, R.G. The Influence of Electrode Porosity on Diffusional Cyclic Voltammetry. *Electroanalysis*, **2008**, *20*, 2387–2394.

[58] Punckt, C.; Pope, M.A.; Aksay, I.A. High Selectivity of Porous Graphene Electrodes Solely Due to Transport and Pore Depletion Effects. *J. Phys. Chem. C*, **2014**, *118*, 22635–22642.

[59] Bae, J.H.; Yu, Y.; Mirkin, M.V. Scanning Electrochemical Microscopy Study of Electron-Transfer Kinetics and Catalysis at Nanoporous Electrodes. *J. Phys. Chem. C*, **2016**, *120*, 20651–20658.

[60] Ji, X.; Banks, C.E.; Crossley, A.; Compton, R.G. Oxygenated Edge Plane Sites Slow the Electron Transfer of the Ferro-/Ferricyanide Redox Couple at Graphite Electrodes. *ChemPhysChem*, **2006**, *7*, 1337–1344.

[61] Poh, H.L.; Pumera, M. Nanoporous Carbon Materials for Electrochemical Sensing. *Chem. – Asian J.*, **2012**, *7*, 412–416.

[62] Nioradze, N.; Chen, R.; Kurapati, N.; Khvataeva-Domanov, A.; Mabic, S.; Amemiya, S. Organic Contamination of Highly Oriented Pyrolytic Graphite As Studied by Scanning Electrochemical Microscopy. *Anal. Chem.*, **2015**, *87*, 4836–4843.

[63] Aziz, M.A.; Park, S.; Jon, S.; Yang, H. Amperometric Immunosensing Using an Indium Tin Oxide Electrode Modified with Multi-Walled Carbon Nanotube and Poly(Ethylene Glycol)–Silane Copolymer. *Chem. Commun.*, **2007**, 2610–2612.

[64] Zudans, I.; Paddock, J.R.; Kuramitz, H.; Maghasi, A.T.; Wansapura, C.M.; Conklin, S.D.; Kaval, N.; Shtoyko, T.; Monk, D.J.; Bryan, S.A.; Hubler, T.L.; Richardson, J.N.; Seliskar, C.J.; Heineman, W.R. Electrochemical and Optical Evaluation of Noble Metal– and Carbon–ITO Hybrid Optically Transparent Electrodes. *J. Electroanal. Chem.*, **2004**, *565*, 311–320.

[65] Hoertz, P.G.; Chen, Z.; Kent, C.A.; Meyer, T.J. Application of High Surface Area Tin-Doped Indium Oxide Nanoparticle Films as Transparent Conducting

Electrodes. *Inorg. Chem.*, **2010**, *49*, 8179–8181.

[66] Gordon, R.G. Criteria for Choosing Transparent Conductors. *MRS Bull.*, **2000**, *25*, 52–57.

[67] Mryasov, O.N.; Freeman, A.J. Electronic Band Structure of Indium Tin Oxide and Criteria for Transparent Conducting Behavior. *Phys. Rev. B*, **2001**, *64*, 233111.

[68] Graberg, T. von; Hartmann, P.; Rein, A.; Gross, S.; Seelandt, B.; Röger, C.; Zieba, R.; Traut, A.; Wark, M.; Janek, J.; Smarsly, B.M. Mesoporous Tin-Doped Indium Oxide Thin Films: Effect of Mesostructure on Electrical Conductivity. *Sci. Technol. Adv. Mater.*, **2011**, *12*, 025005.

[69] Punckt, C.; Pope, M.A.; Aksay, I.A. On the Electrochemical Response of Porous Functionalized Graphene Electrodes. *J. Phys. Chem. C*, **2013**, *117*, 16076–16086.

[70] Park, S.; Song, Y.J.; Han, J.-H.; Boo, H.; Chung, T.D. Structural and Electrochemical Features of 3D Nanoporous Platinum Electrodes. *Electrochimica Acta*, **2010**, *55*, 2029–2035.

[71] Bard, A.J. *Electrochemical Methods: Fundamentals and Applications*; Wiley, **2001**.

[72] Fabregat-Santiago, F.; Garcia-Belmonte, G.; Bisquert, J.; Zaban, A.; Salvador, P. Decoupling of Transport, Charge Storage, and Interfacial Charge Transfer in the Nanocrystalline TiO2/Electrolyte System by Impedance Methods. *J. Phys. Chem. B*, **2002**, *106*, 334–339.

[73] Brug, G.J.; van den Eeden, A.L.G.; Sluyters-Rehbach, M.; Sluyters, J.H. The Analysis of Electrode Impedances Complicated by the Presence of a Constant Phase Element. *J. Electroanal. Chem. Interfacial Electrochem.*, **1984**, *176*, 275–295.

[74] Lasia, A. *Electrochemical Impedance Spectroscopy and Its Applications*; Springer-Verlag: New York, **2014**.

[75] Fosdick, S.E.; Knust, K.N.; Scida, K.; Crooks, R.M. Bipolar Electrochemistry.

Angew. Chem. Int. Ed., **2013**, *52*, 10438–10456.

[76] Loget, G.; Zigah, D.; Bouffier, L.; Sojic, N.; Kuhn, A. Bipolar Electrochemistry: From Materials Science to Motion and Beyond. *Acc. Chem. Res.*, **2013**, *46*, 2513–2523.

[77] Chow, K.-F.; Mavré, F.; Crooks, J.A.; Chang, B.-Y.; Crooks, R.M. A Large-Scale, Wireless Electrochemical Bipolar Electrode Microarray. *J. Am. Chem. Soc.*, **2009**, *131*, 8364–8365.

[78] Hu, S.; Gao, J. Dynamic Bipolar Electrode Array for Visualized Screening of Electrode Materials in Light-Emitting Electrochemical Cells. *ACS Appl. Mater. Interfaces*, **2019**, *11*, 1117–1124.

[79] Eßmann, V.; Santana Santos, C.; Tarnev, T.; Bertotti, M.; Schuhmann, W. Scanning Bipolar Electrochemical Microscopy. *Anal. Chem.*, **2018**, *90*, 6267–6274.

[80] Wu, M.-S.; Liu, Z.; Shi, H.-W.; Chen, H.-Y.; Xu, J.-J. Visual Electrochemiluminescence Detection of Cancer Biomarkers on a Closed Bipolar Electrode Array Chip. *Anal. Chem.*, **2015**, *87*, 530–537.

[81] Lin, X.; Zheng, L.; Gao, G.; Chi, Y.; Chen, G. Electrochemiluminescence Imaging-Based High-Throughput Screening Platform for Electrocatalysts Used in Fuel Cells. *Anal. Chem.*, **2012**, *84*, 7700–7707.

[82] Xu, W.; Fu, K.; Bohn, P.W. Electrochromic Sensor for Multiplex Detection of Metabolites Enabled by Closed Bipolar Electrode Coupling. *ACS Sens.*, **2017**, *2*, 1020–1026.

[83] Guerrette, J.P.; Percival, S.J.; Zhang, B. Fluorescence Coupling for Direct Imaging of Electrocatalytic Heterogeneity. *J. Am. Chem. Soc.*, **2013**, *135*, 855–861.

[84] Zhang, X.; Ding, S.-N. Graphite Paper-Based Bipolar Electrode Electrochemiluminescence Sensing Platform. *Biosens. Bioelectron.*, **2017**, *94*, 47–55.

[85] Sentic, M.; Milutinovic, M.; Kanoufi, F.; Manojlovic, D.; Arbault, S.; Sojic, N.

Mapping Electrogenerated Chemiluminescence Reactivity in Space: Mechanistic Insight into Model Systems Used in Immunoassays. *Chem. Sci.*, **2014**, *5*, 2568–2572.

[86] Sentic, M.; Arbault, S.; Goudeau, B.; Manojlovic, D.; Kuhn, A.; Bouffier, L.; Sojic, N. Electrochemiluminescent Swimmers for Dynamic Enzymatic Sensing. *Chem. Commun.*, **2014**, *50*, 10202–10205.

[87] Feng, Q.-M.; Pan, J.-B.; Zhang, H.-R.; Xu, J.-J.; Chen, H.-Y. Disposable Paper-Based Bipolar Electrode for Sensitive Electrochemiluminescence Detection of a Cancer Biomarker. *Chem. Commun.*, **2014**, *50*, 10949–10951.

[88] Arora, A.; Eijkel, J.C.T.; Morf, W.E.; Manz, A. A Wireless Electrochemiluminescence Detector Applied to Direct and Indirect Detection for Electrophoresis on a Microfabricated Glass Device. *Anal. Chem.*, **2001**, *73*, 3282–3288.

[89] Zhan, W.; Alvarez, J.; Crooks, R.M. Electrochemical Sensing in Microfluidic Systems Using Electrogenerated Chemiluminescence as a Photonic Reporter of Redox Reactions. *J. Am. Chem. Soc.*, **2002**, *124*, 13265–13270.

[90] Chow, K.-F.; Mavré, F.; Crooks, R.M. Wireless Electrochemical DNA Microarray Sensor. *J. Am. Chem. Soc.*, **2008**, *130*, 7544–7545.

[91] Wu, M.-S.; Yuan, D.-J.; Xu, J.-J.; Chen, H.-Y. Electrochemiluminescence on Bipolar Electrodes for Visual Bioanalysis. *Chem. Sci.*, **2013**, *4*, 1182–1188.

[92] Eßmann, V.; Jambrec, D.; Kuhn, A.; Schuhmann, W. Linking Glucose Oxidation to Luminol-Based Electrochemiluminescence Using Bipolar Electrochemistry. *Electrochem. Commun.*, **2015**, *50*, 77–80.

[93] El Kasmi, A.; Leopold, M.C.; Galligan, R.; Robertson, R.T.; Saavedra, S.S.; El Kacemi, K.; Bowden, E.F. Adsorptive Immobilization of Cytochrome c on Indium/Tin Oxide (ITO): Electrochemical Evidence for Electron Transfer-Induced Conformational Changes. *Electrochem. Commun.*, **2002**, *4*, 177–181.

[94] Moore, E.; O'Connell, D.; Galvin, P. Surface Characterisation of Indium-Tin Oxide Thin Electrode Films for Use as a Conducting Substrate in DNA Sensor

Development. *Thin Solid Films*, **2006**, *515*, 2612–2617.

[95] Lin, J.; Qu, W.; Zhang, S. Disposable Biosensor Based on Enzyme Immobilized on Au–Chitosan-Modified Indium Tin Oxide Electrode with Flow Injection Amperometric Analysis. *Anal. Biochem.*, **2007**, *360*, 288–293.

[96] Tian, H.; Jia, M.; Zhang, M.; Hu, J. Nonenzymatic Glucose Sensor Based on Nickel Ion Implanted-Modified Indium Tin Oxide Electrode. *Electrochimica Acta*, **2013**, *96*, 285–290.

[97] Rashid, J.I.A.; Yusof, N.A.; Abdullah, J.; Hashim, U.; Hajian, R. The Utilization of SiNWs/AuNPs-Modified Indium Tin Oxide (ITO) in Fabrication of Electrochemical DNA Sensor. *Mater. Sci. Eng. C*, **2014**, *45*, 270–276.

[98] Reuillard, B.; Ly, K.H.; Hildebrandt, P.; Jeuken, L.J.C.; Butt, J.N.; Reisner, E. High Performance Reduction of H2O2 with an Electron Transport Decaheme Cytochrome on a Porous ITO Electrode. *J. Am. Chem. Soc.*, **2017**, *139*, 3324–3327.

[99] Hwang, D.-W.; Lee, S.; Seo, M.; Chung, T.D. Recent Advances in Electrochemical Non-Enzymatic Glucose Sensors – A Review. *Anal. Chim. Acta*, **2018**, *1033*, 1–34.

[100] Seo, M.; Bae, J.H.; Hwang, D.W.; Kwak, B.; Yun, J.; Lim, S.Y.; Chung, T.D. Catalytic Electron Transfer at Nanoporous Indium Tin Oxide Electrodes. *Electrochimica Acta*, **2017**, *258*, 90–97.

[101] Wei, M.-Y.; Huang, R.; Guo, L.-H. High Catalytic Activity of Indium Tin Oxide Nanoparticle Modified Electrode towards Electro-Oxidation of Ascorbic Acid. *J. Electroanal. Chem.*, **2012**, *664*, 156–160.

[102] Mierzwa, M.; Lamouroux, E.; Vakulko, I.; Durand, P.; Etienne, M. Electrochemistry and Spectroelectrochemistry with Electrospun Indium Tin Oxide Nanofibers. *Electrochimica Acta*, **2016**, *202*, 55–65.

[103] Aziz, M.A.; Mahfoz, W.; Nasiruzzaman Shaikh, M.; Zahir, M.H.; Al-Betar, A.-R.; Oyama, M.; Theleritis, D.; Yamani, Z.H. Preparation of Indium Tin Oxide Nanoparticle-Modified 3-Aminopropyltrimethoxysilane-

Functionalized Indium Tin Oxide Electrode for Electrochemical Sulfide Detection. *Electroanalysis*, **2017**, *29*, 1683–1690.

[104] McCrory, C.C.L.; Jung, S.; Peters, J.C.; Jaramillo, T.F. Benchmarking Heterogeneous Electrocatalysts for the Oxygen Evolution Reaction. *J. Am. Chem. Soc.*, **2013**, *135*, 16977–16987.

[105] Wang, T.; Zhu, H.; Zhuo, J.; Zhu, Z.; Papakonstantinou, P.; Lubarsky, G.; Lin, J.; Li, M. Biosensor Based on Ultrasmall MoS2 Nanoparticles for Electrochemical Detection of H2O2 Released by Cells at the Nanomolar Level. *Anal. Chem.*, **2013**, *85*, 10289–10295.

[106] Mavré, F.; Chow, K.-F.; Sheridan, E.; Chang, B.-Y.; Crooks, J.A.; Crooks, R.M. A Theoretical and Experimental Framework for Understanding Electrogenerated Chemiluminescence (ECL) Emission at Bipolar Electrodes. *Anal. Chem.*, **2009**, *81*, 6218–6225.

[107] Oja, S.M.; Zhang, B. Electrogenerated Chemiluminescence Reporting on Closed Bipolar Microelectrodes and the Influence of Electrode Size. *ChemElectroChem*, **2016**, *3*, 457–464.

국문 초록

효율적인 에너지 전환 장치 혹은 저장 장치, 그리고 센서 등에 대한 수요가 높아짐에 따라, 이들의 성능을 결정짓는 전기화학 촉매에 대한 연구가 활발히 진행되고 있다. 이러한 촉매 연구들은 촉매 효율을 최대한으로 끌어올리면서 동시에 귀금속 재료를 줄이는 방향으로 이루어지고 있다. 이러한 맥락에서 촉매들을 나노구조체로 제작하는 전략 또한 전극 표면적을 늘리거나 표면 자체의 촉매성을 높이려는 의도로 자주 쓰인다.

그 중에서도 나노다공성 구조의 전극들은 부피 대비 표면적 증가 및 표면 활성화 측면에서 주목받는 촉매 물질이다. 하지만 나노다공성 전극의 표면 성질로부터 파생되는 촉매 효과 외에도, 나노동공 구조 내부 반응종의 갇힘 효과에 의한 추가적인 촉매 효과가 있을 것이라는 주장이 제기된 바가 있다. 이러한 '나노 갇힘 효과' 연구들은 주로 귀금속 재료의 나노다공성 전극을 이용하여 연구가 진행되어 왔다. 본 연구에서는 낮은 촉매성을 가지는 인듐 주석 산화물 (indium tin oxide, ITO)을 재료로 하여 나노다공성 층의 두께를 변화시켜가면서 나노 갇힘 효과를 관찰하였다. 또한 나노 갇힘 효과에 바탕한 구조 개조의 촉매 개발 응용 가능성을 센서 성능으로 보여주었다.

챕터 1 에서는 나노다공성 인듐 주석 산화물 전극을 도입하여 하나의 전자 전달이 가속화됨을 관찰하였고, 나노다공성 전극에서의 촉매 메커니즘을 구조 효과 측면에서 살펴보았다. 이를 위해, 촉매 효과가 느리다고 알려진 인듐 주석 산화물을 전극 재료로 택하였으며,

나노다공성 층 두께에 따른 전자전달 반응 빠르기를 관찰함으로써 전극 표면 성질로부터 파생되는 촉매 효과를 상쇄시킬 수 있었다. 이로부터 $Fe^{2+/3+}$ 전자 전달 빠르기가 두꺼운 나노다공성 층에서 점차 증가하는 것을 보았으며, 이는 나노다공성 구조로부터 기인한 것으로 분석하였다.

챕터 2 에서는 나노다공성 인듐 주석 산화물을 바이폴러 전극 (bipolar electrode, BPE) 센서에 도입함으로써 과산화수소에 대한 분석 능력이 향상됨을 관찰하였다. 과산화수소 농도에 따른 적정 곡선을 통해 BPE 센서에 나노다공성 구조를 도입할 경우, 그렇지 않은 평탄한 전극에 비해 감도가 매우 크게 향상하였으며, 약한 작동 전압에서도 효율적인 측정을 할 수 있었다.

핵심 단어: 전기화학 촉매, 나노다공성 전극, 나노 갇힘 효과, 전기화학 임피던스 분광학, 바이폴러 전극

학번: 2014-21241